Cloud-Resolving Model Applied to Nowcasting: An Evaluation of Radar Data Assimilation and Microphysics Parameterization

EDER P. VENDRASCO,[a] LUIZ A. T. MACHADO,[a,b] BRUNO Z. RIBEIRO,[c] EDMILSON D. FREITAS,[d] RUTE C. FERREIRA,[a] AND RENATO G. NEGRI[a]

[a] *Center for Weather Forecast and Climate Studies, National Institute for Space Research (CPTEC/INPE), Cachoeira Paulista, São Paulo, Brazil;* [b] *Multiphase Chemistry Department, Max Planck Institute for Chemistry, Mainz, Germany;* [c] *Department of Atmospheric and Environmental Sciences, University at Albany, State University of New York, Albany, New York;* [d] *Institute of Astronomy, Geophysics and Atmospheric Sciences, University of Sao Paulo (IAG/USP), São Paulo, Brazil*

(Manuscript received 7 February 2020, in final form 7 September 2020)

ABSTRACT: This research explores the benefits of radar data assimilation for short-range weather forecasts in southeastern Brazil using the Weather Research and Forecasting (WRF) Model's three-dimensional variational data assimilation (3DVAR) system. Different data assimilation options are explored, including the cycling frequency, the number of outer loops, and the use of null-echo assimilation. Initially, four microphysics parameterizations are evaluated (Thompson, Morrison, WSM6, and WDM6). The Thompson parameterization produces the best results, while the other parameterizations generally overestimate the precipitation forecast, especially WDSM6. Additionally, the Thompson scheme tends to overestimate snow, while the Morrison scheme overestimates graupel. Regarding the data assimilation options, the results deteriorate and more spurious convection occurs when using a higher cycling frequency (i.e., 30 min instead of 60 min). The use of two outer loops produces worse precipitation forecasts than the use of one outer loop, and the null-echo assimilation is shown to be an effective way to suppress spurious convection. However, in some cases, the null-echo assimilation also removes convective clouds that are not observed by the radar and/or are still not producing rain, but have the potential to grow into an intense convective cloud with heavy rainfall. Finally, a cloud convective mask was implemented using ancillary satellite data to prevent null-echo assimilation from removing potential convective clouds. The mask was demonstrated to be beneficial in some circumstances, but it needs to be carefully evaluated in more cases to have a more robust conclusion regarding its use.

KEYWORDS: Nowcasting; Numerical weather prediction/forecasting; Cloud resolving models; Data assimilation

1. Introduction

Accurate short-term high-resolution precipitation forecast has been a challenge over the last few decades. Computing power has increased, allowing an increase in model grid resolution, but the accuracy in predicting the time and position of a particular convective cell is still a challenge, especially in the first forecast hours. One of the reasons for this low accuracy at the very beginning of the forecast is the well-known spinup problem (Illari 1987). This problem becomes more relevant when performing short-term weather forecasts (1–6 h). For precipitation predictions of up to 2–3 h, Lagrangian advection of radar echoes usually performs better than numerical weather prediction (NWP) (Lin et al. 2005; Sun et al. 2014). Of course, the prediction performance depends on the precipitation system type (i.e., less organized convection has a forecast range much shorter than those of well-organized systems) (Zipser 1990). In the range between approximately 3 and 6 h, there is a gap in performance between extrapolation methods and dynamic numerical models. To bridge this gap, many studies have been performed to reduce the spinup of numerical models (Sun et al. 2014). One of the best ways to improve the model accuracy at the very beginning of a precipitation forecast is to better represent the model's initial conditions (Stensrud et al. 2013), which can be accomplished by performing convective-scale data assimilation (DA) (Sun et al. 2014). Data assimilation is a technique for generating accurate images of the true state of the atmosphere at a given time in which the observed information is accumulated into the model state by taking advantage of consistency constraints with laws of time evolution and physical properties. A crucial advantage of NWP models with DA compared to nowcasting tools (e.g., extrapolation of radar echoes) is that DA not only adds the current data into the NWP model but also initializes convective-scale events (Sokol 2011). A logical approach used for nowcasting is to blend radar echo extrapolation with a numerical model to generate a seamless 0–6-h forecast (Sun et al. 2014). However, extrapolation accuracy is strongly reduced with time, and a blended forecast relies entirely on numerical models after 3–4 h.

Initial conditions play a crucial role in numerical weather prediction (NWP). For high-resolution forecasts, the model needs to be initialized with observations that describe not only the large-scale features, but also the convective-scale phenomena. Understanding how to assimilate observations at the convective scale, resolving the dynamic process relevant to predicting convection evolution and dealing with rapid error growth is a huge challenge. Doppler radar observations have been used in complex DA systems to improve the initial condition of high-resolution models since these observations are almost the only source of three-dimensional data at this scale

Corresponding author: Eder Paulo Vendrasco, eder.vendrasco@inpe.br

DOI: 10.1175/WAF-D-20-0017.1

(Aksoy et al. 2009). Reflectivity and radial velocities from Doppler radar have been successfully used in complex DA to improve the initial conditions for convection-permitting models (e.g., Gao et al. 2004; Kong et al. 2018; Ming et al. 2009; Tong et al. 2016; Vendrasco et al. 2016; Wang et al. 2013; Xiao et al. 2007). More recently, polarimetric variables have also been used in DA systems (e.g., Carlin et al. 2017; Kawabata et al. 2018; Li et al. 2017; Wolfensberger and Berne 2018). Although many studies have shown improvements in precipitation forecasts due to radar DA, it is still a challenge to extract as much information as possible from observations while maintaining the large-scale background balance. Vendrasco et al. (2016) have shown that constraining the cost function with a large-scale analysis can alleviate this problem. Also, the choice of the cycling frequency can play an important role in the analysis and forecast quality, and the best analysis will not automatically produce the best forecast. Pan and Wang (2019) studied the assimilation frequency of radar data and they concluded that a higher DA frequency can produce a more intense cold pool and rear inflow jets but does not necessarily lead to a better forecast. Besides, Tong et al. (2016) studied the best cycling strategy to assimilate radar data and found that performing three 1-h cycles before the analysis time results in better accuracy than performing just one 3-h cycle.

Another important aspect that directly affects precipitation in high-resolution forecasts is the microphysical parameterization. Many approaches are considered to parameterize the in-cloud process, and these approaches can be categorized into two schemes: bulk and bin parameterizations. Bin schemes aim to calculate microphysics as accurately and generally as possible, and divide microphysical particles with different sizes into bins to compute the evolution of each bin separately. Thus, the particle size distribution (PSD) is an output instead of the moments provided by bulk schemes. Although bin schemes are much more detailed and precise, these methods are very expensive computationally and are not feasible in operational NWP models. Bulk schemes can be classified by the number of moments (predicted variables) that are included in the parameterization. The most common bulk parameterizations are those with single moments [e.g., Ferrier (Ferrier et al. 2002); WSM6 (Hong and Lim 2006); Thompson (Thompson et al. 2008)], which predict only the mass of the particles, and the double moment bulk schemes, which also predict the total number concentration [e.g., WDM6 (Lim and Hong 2010); Morrison (Morrison et al. 2009)]. Although uncommon in operational NWP models, there are also developments in bulk schemes regarding the third moment, which also provides a prediction for the reflectivity (e.g., (Milbrandt and Yau 2005). Many works have shown the impact of microphysical parameterization on high-resolution precipitation forecasting (Fovell et al. 2009; Morrison et al. 2009; Cheng et al. 2011; Wu et al. 2013; Grabowski 2014; Mohan et al. 2019); however, only a few have discussed the impact of microphysical parameterization on radar DA (Yussouf et al. 2013; Putnam et al. 2017). Although all the bulk microphysics parameterizations solve similar processes, the production of rain and its timing can also be distinct. The question that arises is: does radar DA have any impact on this behavior?

The goal of this paper is to evaluate the performance of the cloud-resolving model for nowcasting applications on intense thunderstorms and provide some evaluations regarding the impact of different radar DA procedures and microphysics parameterization.

The paper is organized as follows: section 2 presents the SOS-CHUVA project and the radar data used in this work and outlines the experimental setup. Additionally, this section briefly describes the Weather Research and Forecasting (WRF) Model three-dimensional variational (3DVAR) DA system employed in this study and the methods for precipitation verification. Section 3 presents the evaluation of the DA procedure based on increments, innovations and residuals and the short-range precipitation forecast for 5 convective cases to show how radar DA and different microphysics impact the precipitation forecast in the first 6 h of leading time. The main results obtained from this study are summarized in section 4.

2. Data and methodology

a. *The SOS-CHUVA campaign*

The SOS-CHUVA campaign occurred in southeastern Brazil between 2016 and 2019. The campaign was a collaborative effort of several Brazilian institutions to better understand severe thunderstorms in the region and improve nowcasting tools and methodologies. SOS-CHUVA is an extension of the CHUVA project (Machado et al. 2014), particularly dedicated to nowcasting. During the experiment, several instruments were installed and operated over a 2-yr period (2016–18) in Campinas, São Paulo, Brazil (Fig. 1), in particular, an X-band polarimetric radar and two other operational S-band radars.

b. *Selection of the cases*

Five cases of intense storms were selected within the radar coverage area during the SOS-CHUVA campaign (Fig. 2). The five cases were chosen based on their intensity and the availability of data, particularly radar data. Additionally, there was an attempt to include cases of convective systems with different morphologies, from organized mesoscale convective systems, such as quasilinear convective systems (QLCS) and storm clusters, to isolated storms. For all the cases, intense weather was reported, including hail, strong winds and/or flooding (see Fig. 2). A synthesis of these cases, as well as the radar data used in the DA system, is shown in Table 1. A more detailed discussion of the events and the synoptic-scale environment is presented in section 3a.

c. *Radar data*

The three radars employed in this study were located in São Roque (23.602°S, 47.094°W, 1147-m altitude; SR), Salesópolis (23.600°S, 45.972°W, 916-m altitude; SL) and Campinas (22.813°S, 47.056°W, 680-m altitude; CP), Brazil; see Fig. 1 and Table 2 for a detailed description of all the radars. Volumetric data are available every 5, 10, and 15 min for the CP, SR, and SL radars, respectively. However, in this study, only the volumetric data from every 30 min were used in the DA cycling process and the forecast evaluation. Each radar has its own

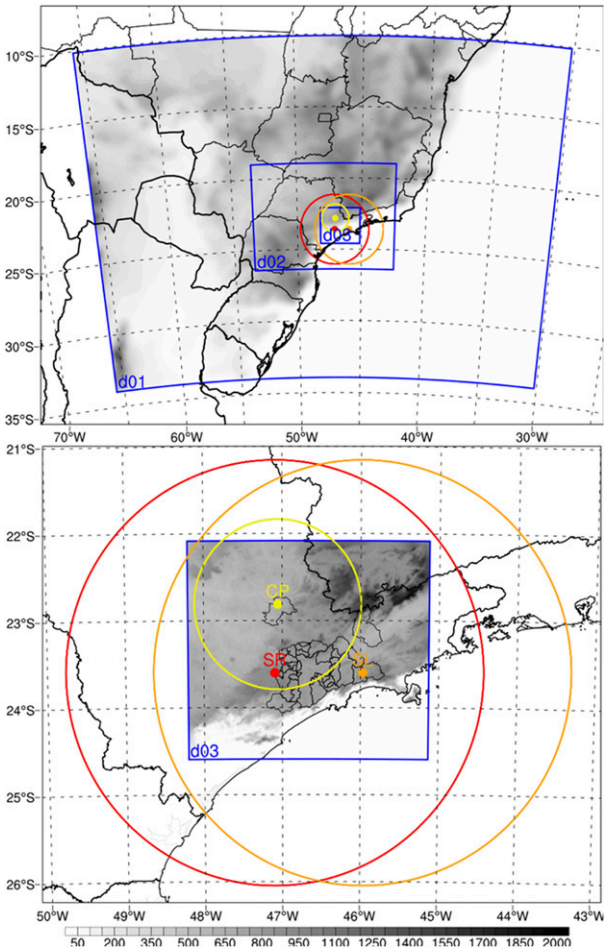

FIG. 1. Map showing the location of the radars used in this study and the WRF domains. (a) Topography (m) from the d01 domain is shaded, and the WRF domains (d01, d02, and d03) are shown along with the radar location (colored dots) and coverage (colored circles). (b) Topography (m) from the d03 WRF domain is shaded, SR is the nonpolarimetric S-band radar located in São Roque (red dot and circle with 250-km radius), SL is the polarimetric S-band radar of Salesopolis (orange dot and circle with 250-km radius), and CP represents the X-band polarimetric radar in Campinas (yellow dot and circle with 100-km radius).

automatic quality control procedure, which includes ground clutter removal. For radars SR and SL, the dealiasing procedure (James and Houze 2001) from Py-ART (Helmus and Collis 2016) was also applied, while the CP radar run in dual-pulse repetition frequency (PRF) mode and the dealiasing procedure was not necessary. Due to the strong attenuation observed on X-band radars, the data from CP radar was corrected by applying the methodology described in (Schneebeli et al. 2012). The ZPHI algorithm (Testud et al. 2000) is also employed in the X-band radars for attenuation correction. After the data were preprocessed, each elevation of the volumetric radar data was interpolated horizontally to a regular grid of 1-km resolution. Finally, the interpolated reflectivity and Doppler wind fields were used to produce profiles to be assimilated.

d. WRF and WRFDA

The model used in the study was the WRF Model with the Advanced Research version of WRF dynamical core (WRF-ARW; Skamarock et al. 2008), version 3.9.1.1, and its 3DVAR DA system (WRFDA-3DVAR), version 3.9.1 (Barker et al. 2004). This system iteratively minimizes the cost function defined by

$$J = J_b + J_o = \frac{1}{2}\mathbf{v}^{\mathrm{T}}\mathbf{v} + \frac{1}{2}(\mathbf{d} - \mathbf{H}'\mathbf{U}\mathbf{v})^{\mathrm{T}}\mathbf{R}^{-1}(\mathbf{d} - \mathbf{H}'\mathbf{U}\mathbf{v}), \qquad (1)$$

where J_b and J_o represent the background (i.e., the previous model forecast) and observation terms, respectively. The term $\mathbf{v}$ is the control variable (CV) defined by $\mathbf{v} = \mathbf{U}^{-1}(\mathbf{x} - \mathbf{x}_b)$, where $\mathbf{U}$ is the decomposition of the background error covariance $\mathbf{B}$ via $\mathbf{B} = \mathbf{U}\mathbf{U}^{\mathrm{T}}$, $\mathbf{x}_b$ is the background variable, $\mathbf{x}$ is the model state and the analysis $\mathbf{x} = \mathbf{x}_a$ represents the a posteriori maximum likelihood or minimum variance estimate of the true state of the atmosphere. The innovation vectors that measure the departure of the observation $\mathbf{y}_0$ from its counterpart computed from the background $\mathbf{x}_b$ are given by $\mathbf{d} = \mathbf{y}_0 - \mathbf{H}(\mathbf{x}_b)$. The term $\mathbf{H}'$ is the linearization of the nonlinear observation operator $\mathbf{H}$, and $\mathbf{R}$ is the observation error covariance matrix.

The operator $\mathbf{H}'$ is obtained by considering the first-order Taylor series expansion of $\mathbf{H}$ and the inner loop procedure solves a minimization algorithm for a quadratic problem (Courtier et al. 1998). The nonlinear aspects of the assimilation problem are solved by the outer loop procedure. The increment is computed and added back to the control variables after the inner loop minimization algorithm to create the updated first guess. Then, the control variable can be modified with each outer loop. Moreover, because of the analysis from the previous outer loop is closer to the observations, some of the rejected observations by the previous outer loop can now pass the quality control in the current outer loop and modify the final analysis. The positive impact of performing outer loops in a 3DVAR framework should be more evident when using nonlinear operators since the outer loops are able to update the linearization around a better state and thus improve the quality of the analysis (Hsiao et al. 2012). Trémolet (2008) *has shown that the outer loop iterations seem to have more impact in 4DVAR than in 3DVAR. Furthermore, Trèmolet's work also shows that the number of outer loops does not change much the humidity variables; however, the highest impact occurs when highly nonlinear observational operators are used.*

Such as in Sun et al. (2016), the CVs used in this study were the velocity components u and v, temperature T, surface pressure Ps, and pseudorelative humidity RHs (where the humidity is divided by the background humidity). The retrieved rainwater mixing ratio obtained from Marshall–Palmer relationship (Marshall and Palmer 1948), instead of the reflectivity itself, is assimilated following the formulation proposed by Wang et al. (2013) to avoid the nonlinearity issues caused by the linearization of the observation operator required by the incremental formulation (Courtier et al. 1994). In addition, ice-phase hydrometeors such as snow and graupel obtained from reflectivity observations are assimilated following the formulation of Gao and Stensrud (2012).

WRFDA also has the capability of assimilating null-echo reflectivity (a region with no precipitating echo within the

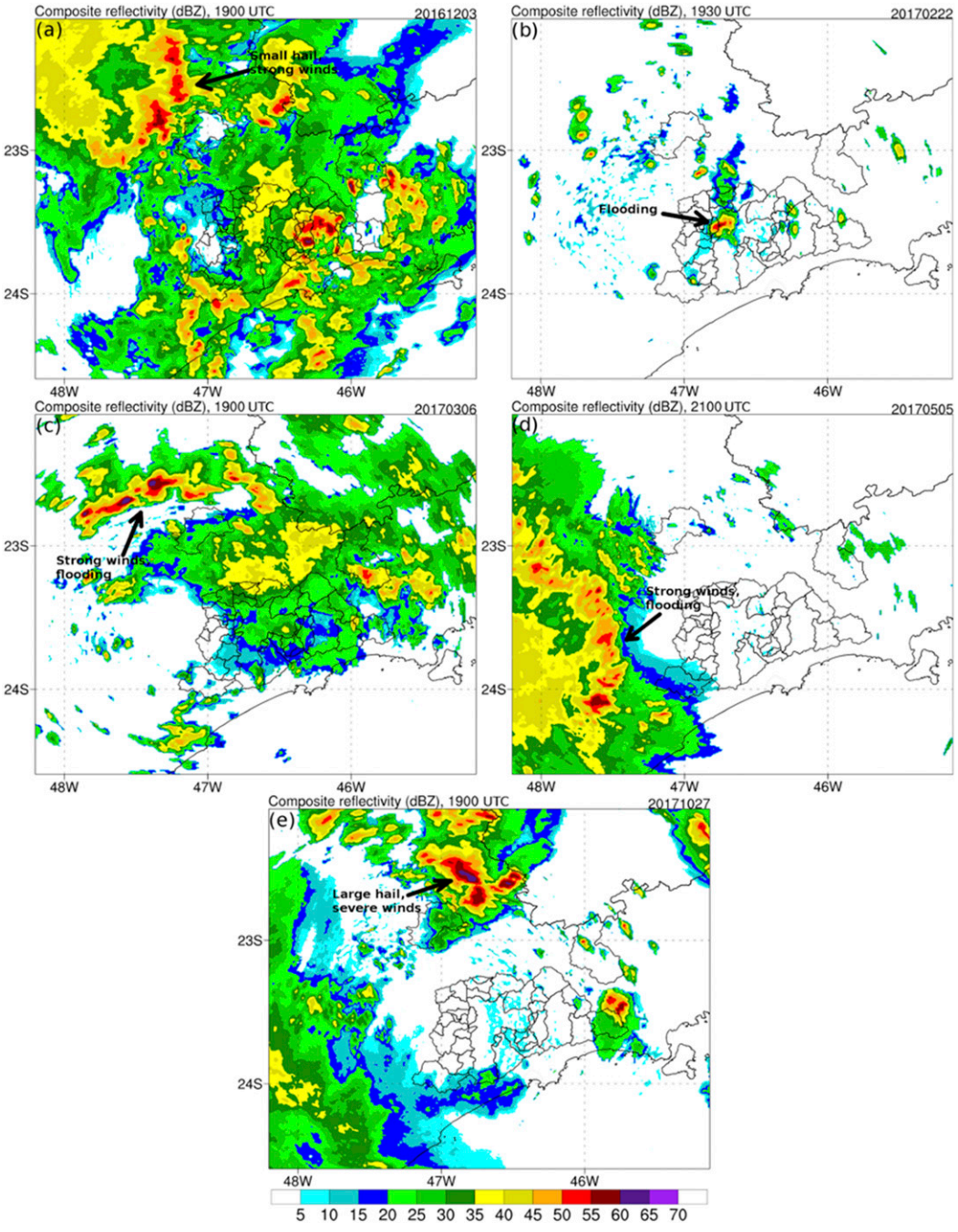

FIG. 2. Composite reflectivity (dBZ) at (a) 1900 UTC 3 Dec 2016, (b) 1930 UTC 22 Feb 2017, (c) 1900 UTC 6 Mar 2017, (d) 2100 UTC 5 May 2017, and (e) 1900 UTC 27 Oct 2017. The reflectivity fields are generated by interpolating the reflectivity from the closest radar to the WRF d03 domain (Fig. 1). The arrows indicate the systems that caused severe weather, which occurred at approximately the times shown in the figures.

radar observation range), the Kyungpook National University (KNU) null-echo scheme (Min et al. 2017). The null-echo information is used to suppress spurious model precipitation. When the null-echo assimilation is employed, excessive humidity and hydrometeor contents, such as wet and dry snow, graupel, and rainwater, are removed based on radar reflectivity by the 3DVAR DA technique. The null-echo assimilation works as follow: it receives from the user all the locations where no precipitation is observed in the radar and it is considered, at these locations, a reflectivity value of -15 dBZ, and if the background has a reflectivity value higher than -15 dBZ, the innovation is calculated and

TABLE 1. Characteristics and data availability for each studied case.

Cases	Dates	Approximate time of severe weather reports	Convective mode	Available radar data
1	3 Dec 2016	1900 UTC	QLCS	SR, SL, and CP
2	22 Feb 2017	1930 UTC	Isolated storm	SR, SL, and CP
3	6 Mar 2017	1900 UTC	Storm cluster	SR and SL
4	5 May 2017	2100 UTC	QLCS	SR, SL, and CP
5	27 Oct 2017	1900 UTC	Storm cluster	SR and CP

considered in the minimization, otherwise, this no precipitation observation is ignored.

The National Meteorological Center (NMC) method (Parrish and Derber 1992) was used in this work to generate background error statistics. A dataset containing 3 months of cold-start 24-h forecasts over the inner domain covering the Southern Hemisphere summer was produced every day starting at 0000 and 1200 UTC. The differences between the 24- and 12-h forecasts valid at the same time were used to calculate the domain-averaged background error statistics. For the radar DA, the error statistics were tuned by halving the length scale and doubling the variance, following Tong et al. (2016). It is assumed that the observation errors are statistically independent of each other, so $\mathbf{R}$ is a diagonal matrix; its diagonal contains the variances of the errors of each observation. The variances for radar data are estimated by applying the standard deviation over the eight neighboring points of each grid point. No special consideration was made regarding the different wavelengths of each radar.

e. *Model configuration*

The WRF model was configured with three one-way nested domains d01, d02, and d03 with 16-, 4-, and 1-km horizontal grid spacing, respectively (see Fig. 1), and 55 layers up to 25 hPa. The purpose of domains d01 and d02 is to provide boundary condition to domain d03 since the data assimilation and all the analysis are performed only for the higher resolution domain, with 1 km grid spacing. For all domains, the physics used were set as follow: for the longwave and shortwave radiation, the rapid radiative transfer model for GCMs (RRTMG; Iacono et al. 2008) was selected, and the employed surface layer scheme was the revised Monin–Obukhov scheme; the surface parameterization scheme was the Noah scheme (Tewari et al. 2004), and the YSU scheme was used to parameterize the planetary boundary layer (Hong et al. 2006). Additionally, only for domain d01, the Kain–Fritsch Cumulus Potential Scheme (Berg et al. 2013) was selected. The Global Forecast System (GFS) forecasts from the National Centers for Environmental Prediction (NCEP) were used as the initial and boundary conditions (IC/BC) for the outermost WRF domain (d01). The GFS is a T1534 global model with 64 vertical levels. The model output is interpolated to a 0.25° resolution grid, which was used in this study. Both the IC/BC and the synoptic-scale analysis of each case used the 1200 UTC GFS runs. All simulations employed the same setup.

Four microphysics schemes were employed: Thompson (Thompson et al. 2008), Morrison (Morrison et al. 2009), WRF double-moment 6-class (WDM6; Lim and Hong 2010), and WRF single-moment 6-class (WSM6; Hong and Lim 2006). The four microphysics schemes combined with two DA methodologies and the schemes without DA resulted in 12 runs for each case. These runs were used to evaluate the impact of microphysics schemes and data assimilation (section 3c). Further DA analysis (sections 3d and 3e) only included the microphysics scheme that provided the best precipitation forecast. Another fourteen experiments exploring different DA options for each case, using only the most appropriate microphysics scheme, were performed. See Tables 3 and 4 for the description of the different configurations.

The cycling methodology is described in Fig. 3. It shows that the d02 domain forecasts (4-km grid spacing) are interpolated to 1 km using the utility NDOWN (Nest-Down) available along with the WRF package to provide initial and boundary condition for one-way nesting simulations. The output of NDOWN is then used as background in WRFDA. For all five cases, four continuously cycled analyses were performed at 1500, 1600, 1700, and 1800 UTC, and then a 6-h forecast ensued. At 1500 UTC the initial conditions for the outermost domain come from the GFS forecasts. The experiments were performed with and without cycles/DA: with cycles and DA

TABLE 2. Radars characteristics.

	São Roque (SR)	Salesópolis (SL)	Campinas (CP)
Wavelength	10.9 cm (S-band)	10.638 cm (S-band)	3.202 cm (X-band)
Beamwidth	2.0°	0.968°	1.3°
Polarimetric	No	Yes	Yes
Doppler	Yes	Yes	Yes
Elevations	15	8	17
Radial resolution	500 m	250 m	200 m
Azimuthal resolution	1°	1°	1°

TABLE 3. Experiments.

Expt	Microphysics	With cycle	With DA
nCYnDA	Morrison/Thompson/WSM6/WDM6	No	No
nCYyDA	Morrison/Thompson/WSM6/WDM6	No	Yes
yCYyDA	Morrison/Thompson/WSM6/WDM6	Yes	Yes

(yCYyDA), without cycles but with DA (nCYyDA), with cycles but with no DA (yCYnDA) and without either (nCYnDA). For the nCYyDA experiments, cycling was not performed. Instead, one-time DA was run at 1800 UTC, and then a 6-h forecast took place. The experiment yCYnDA is similar to the situation where the model is run for 3 h before the time of the forecast initialization (1800 UTC) with an hourly BC update.

f. Statistical verification

Several statistical indices were calculated using the composite reflectivity field generated by the simulations and the composite reflectivity field observed by the radar. For the sake of comparison, the radar composite reflectivity was interpolated into the model grid at 1 km horizontal grid spacing. The contingency table was used to evaluate the simulation reflectivity field with respect to the observed reflectivity field. The total numbers of hits, misses, false alarms and correct negatives in the domain were used to calculate the false alarm ratio [FAR; Eq. (2)] and the probability of detection [POD; Eq. (3)]. The threshold of 0.1 dBZ was used to obtain the hits, misses, false alarms, and correct negatives:

$$\mathrm{FAR} = \frac{\text{false alarms}}{\text{false alarms} + \text{hits}}, \tag{2}$$

$$\mathrm{POD} = \frac{\text{hits}}{\text{hits} + \text{misses}}. \tag{3}$$

The other indices used to evaluate the simulations were the root-mean-square error [RMSE; Eq. (4)] and the fractional skill score [FSS; Eq. (5); Roberts and Lean (2008); Skok and Roberts (2016)]:

$$\mathrm{RMSE} = \sqrt{\frac{1}{N}\sum_{k=1}^{N}(F_k - O_k)^2}, \tag{4}$$

where F and O represent the forecast and observed reflectivity fields, respectively, the k subscript represents the kth grid point, and N is the total number of grid points, and

$$\mathrm{FSS} = 1 - \frac{\mathrm{FBS}}{\mathrm{FBS}_w} = 1 - \frac{\frac{1}{N}\sum_{k=1}^{N}\left(P_{F(k)} - P_{O(k)}\right)^2}{\frac{1}{N}\left[\sum_{k=1}^{N}\left(P_{F(k)}^2 + P_{O(k)}^2\right)\right]}, \tag{5}$$

where FBS and FBS$_w$ are the fractional Brier score and the worst possible FBS that can be obtained from observation and forecast fractions, respectively. The terms $P_{F(k)}$ and $P_{O(k)}$ are the fractional coverages of reflectivity for the kth grid point that exceeds a given threshold for the forecast and observation, respectively. The term N is the total number of grid points in the domain. The $P_{F(k)}$ and $P_{O(k)}$ terms are calculated over a square of 25 grid points (i.e., considering a radius of influence of 2 grid points). The more grid points are considered, the higher should be the FSS; however, the evaluation of localized convection is compromised.

RMSE was calculated only for grid points where both observations and forecasts were above 0.1 dBZ and the FSS threshold was 10 dBZ. All the statistical indices considered only grid points within the 1-km domain area.

TABLE 4. Experiments part 2. All experiments were performed using the Thompson microphysics.

Expt	With cycle	With DA	Cycle period	Outer loop	Null-echo
nCYnDA	No	No	—	—	—
yCYnDA60M	Yes	No	60	—	—
nCYyDA1OLnNE	No	Yes	—	1	No
nCYyDA2OLnNE	No	Yes	—	2	No
nCYyDA1OLyNE	No	Yes	—	1	Yes
nCYyDA2OLyNE	No	Yes	—	2	Yes
yCYyDA60M1OLnNE	Yes	Yes	60	1	No
yCYyDA60M2OLnNE	Yes	Yes	60	2	No
yCYyDA60M1OLyNE	Yes	Yes	60	1	Yes
yCYyDA60M2OLyNE	Yes	Yes	60	2	Yes
yCYyDA30M1OLnNE	Yes	Yes	30	1	No
yCYyDA30M2OLnNE	Yes	Yes	30	2	No
yCYyDA30M1OLyNE	Yes	Yes	30	1	Yes
yCYyDA30M2OLyNE	Yes	Yes	30	2	Yes

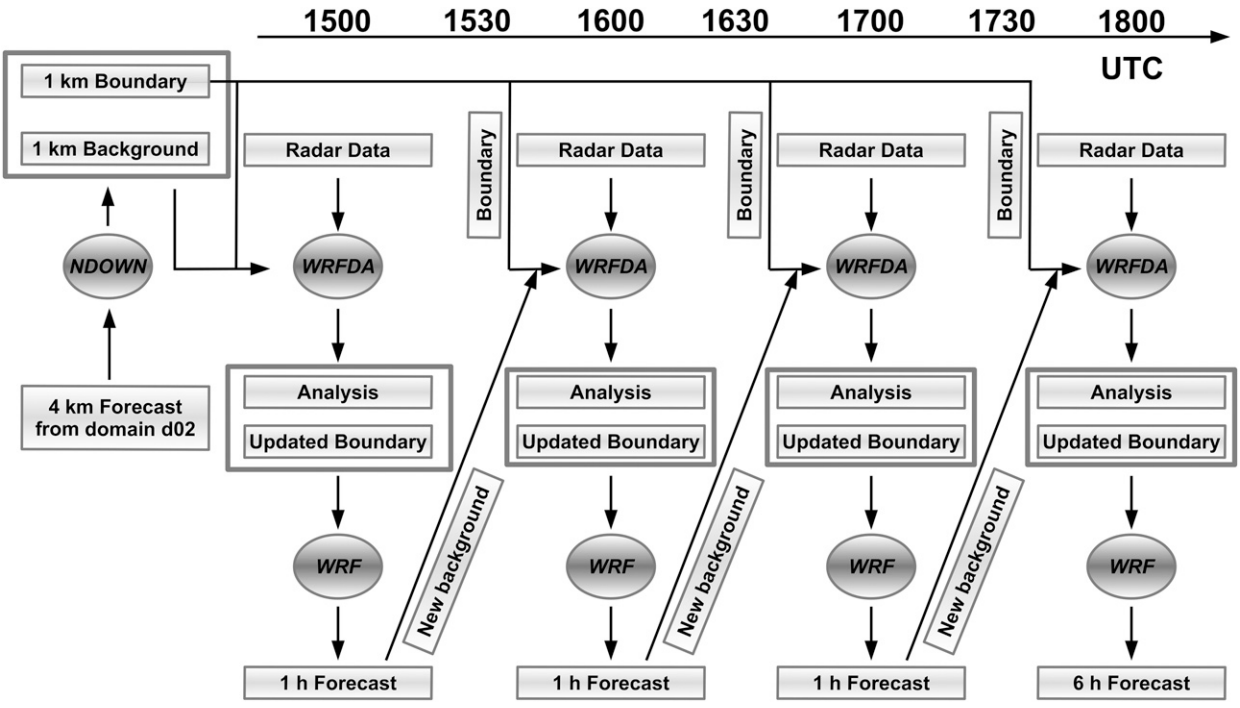

FIG. 3. Schematic diagram of the 60-min cycling strategy. For the 30-min cycle, data assimilation is also performed at 1530, 1630, and 1730 UTC.

3. Results

a. Case description and synoptic-scale environment

Figure 2 shows the composite radar reflectivity of the five cases used in this study for the domain d03 (Fig. 1). The times shown in Fig. 2 are approximately when severe weather was reported at the surface, as indicated in the figure. The cases vary from mature quasilinear convective systems (QLCS) (Figs. 2a,d) to isolated thunderstorms (Fig. 2b). This variation is an important characteristic of the cases selected because it shows that the results of this research evaluate intense events with different types of convective organization. The 3 December 2016 case (Fig. 2a) is characterized by a large number of storms over domain d03, including a QLCS in the northern part of the area that was attributed to several reports of severe winds in the Campinas region. Isolated storms formed over the São Paulo metropolitan region in the afternoon of 22 February 2017 (Fig. 2b) and caused hail and flash flooding in the area. On 6 March 2017 (Fig. 2c), a large area of precipitation covered most of the study region, with embedded severe storms in the northern sector causing hail and strong winds. The second QLCS among the studied cases occurred on 5 May 2017 (Fig. 2d) and was responsible for multiple severe wind reports and flooding. Finally, on 27 October 2017 (Fig. 2e), severe storms formed north of Campinas, presenting Doppler velocity couplets indicating rotation during several radar scans (not shown), that were responsible for strong winds and hail. This event was classified as a supercell.

The synoptic-scale 500-hPa configuration (vorticity and winds at 500 hPa) at 1800 UTC for each case is shown in Fig. 4. At 1800 UTC 3 December 2016 (Fig. 4a), a cyclonic vorticity maximum was located upstream of the study region that caused lifting due to cyclonic vorticity advection (not shown). This trough was associated with cold air advection at 500 hPa, which contributed to the increase of instability with time. The relatively strong 500-hPa flow (15–20 m s^{-1}) contributed to high wind shear and convective organization (Fig. 2a). Weak midlevel flow predominated in the study region during the isolated storms on 22 February 2017 (Fig. 4b). The absence of a source of synoptic-scale lifting suggests that these storms formed due to radiative surface heating and the increase in thermodynamic instability during the afternoon associated with the penetration of the sea breeze. The case of 6 March 2017 (Fig. 4c) also occurred under weak midlevel flow, which contributed to the slow storm movement and the occurrence of flooding. Similar to the 3 December 2016 case, on 5 May 2017 (Fig. 4d), a synoptic-scale trough upstream of the study region caused ascent and midlevel cold advection and contributed to intensify the wind shear and organize the QLCS. The storms that occurred on 27 October 2017 formed downstream of a midlevel vorticity maximum embedded in a strong zonal flow (Fig. 4e).

b. Increments and OMB/OMA profiles

This section shows the impact of radar DA on the analysis (i.e., the output from the DA system) with each microphysics scheme. Thus, only experiments with DA are considered (i.e., nCYyDA and yCYyDA from Table 3). The first question addressed regards the DA behavior for each microphysics parameterization.

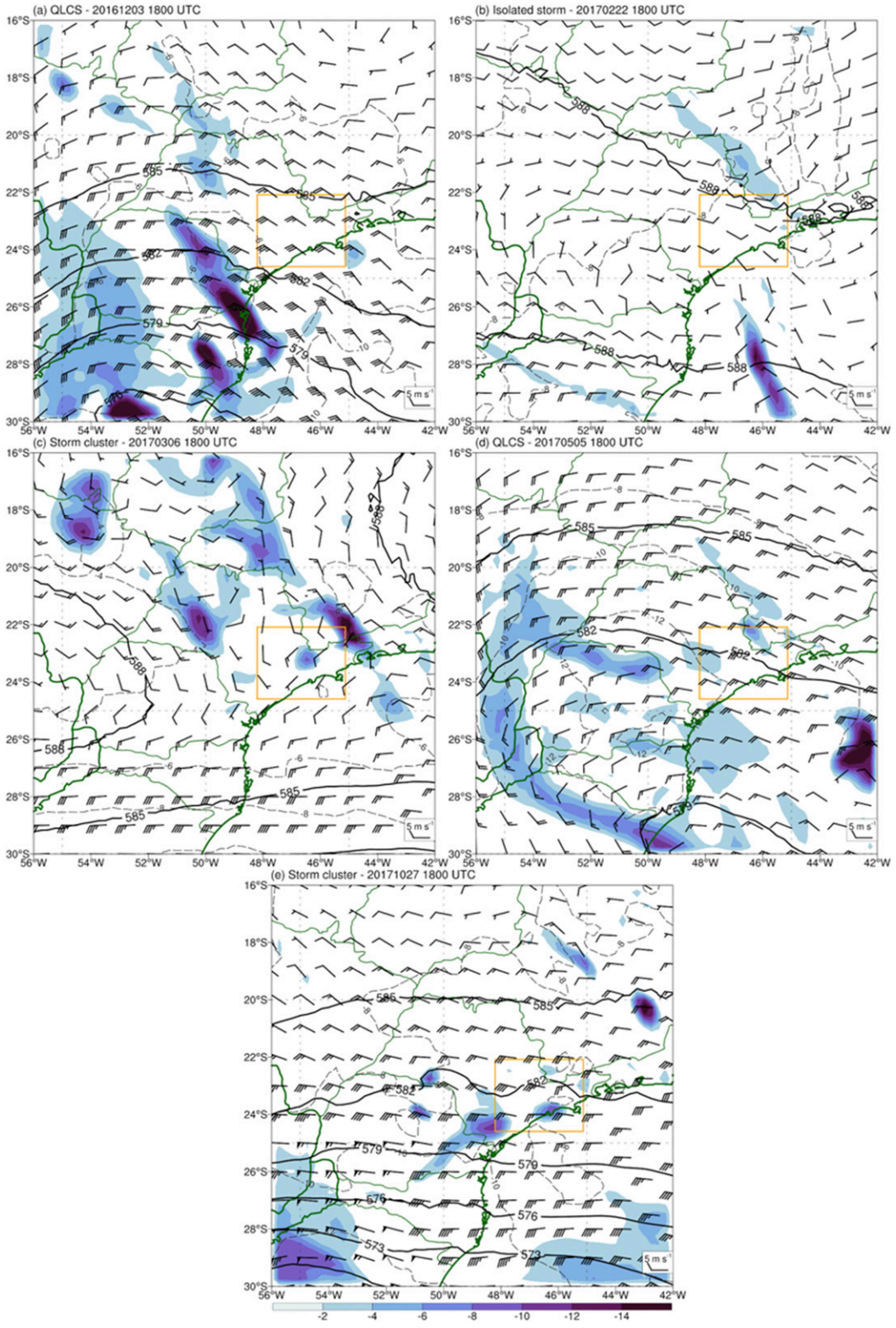

FIG. 4. GFS analysis of 500-hPa relative vertical vorticity (10^{-5} s^{-1}; shaded), geopotential height (dam; black contours every 3 dam), temperature (°C; gray dashed contours every 2°C), and winds (m s^{-1}; pennant is 25 m s^{-1}, full barb is 5 m s^{-1}, and half barb is 2.5 m s^{-1}) at 1800 UTC (a) 3 Dec 2016, (b) 22 Feb 2017, (c) 6 Mar 2017, (d) 5 May 2017, and (e) 27 Oct 2017. The d03 domain is shown in orange.

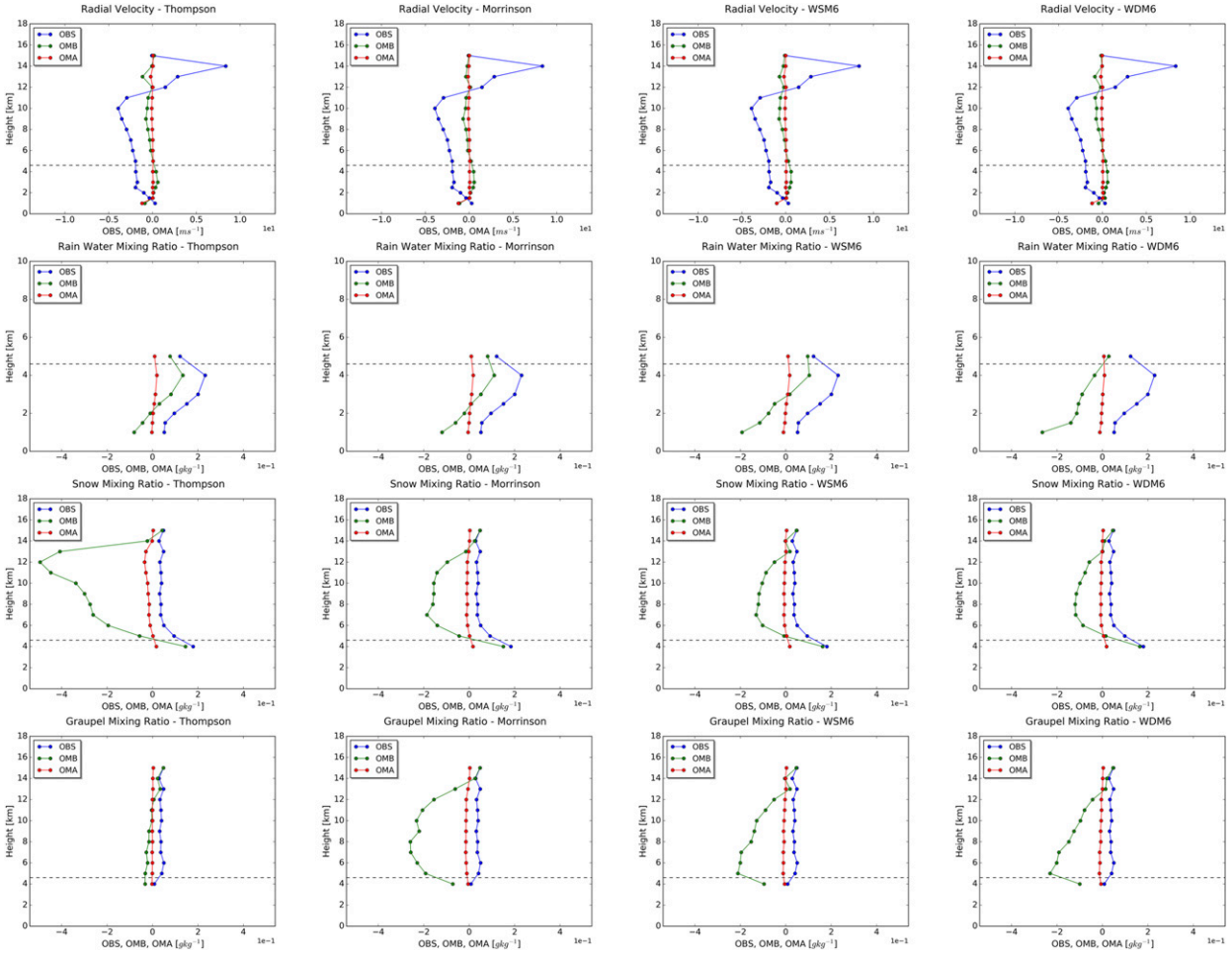

FIG. 5. Averaged vertical profiles of observation (OBS), innovation [observation minus background (OMB)], and residual [observation minus analysis (OMA)]. The average is performed over the entire grid where radar data are available and for all five cases. The freezing level is also shown by the dashed line.

Figure 5 shows the averaged vertical profiles of observation, innovation [observation minus background (OMB)] and residual [observation minus analysis (OMA)] for radial velocity and rainwater, snow, and graupel mixing ratios. The first remarkable feature is that the residual is always close to zero over the entire profile. This means that the DA is capable of removing almost all the innovation and, thus, brings the background closer to the observations. Another interesting finding is that while almost no difference is observed among the microphysics in the radial velocity profile and just a small difference exists in the rainwater mixing ratio, the snow and graupel profiles present the greatest differences. It is important to state that the microphysics observations are estimated using the relationships of Gao and Stensrud (2012) employed in the WRFDA. Figure 5 clearly shows that after four cycles the Thompson microphysics parameterization predicts much more snow than the other parameterizations. On the other hand, Morrison microphysics produces much more graupel than it was estimated from radar, followed by WSM6 and WDM6. The overestimation of snow and graupel by Thompson and Morrison, respectively, agrees with the results of Bao et al. (2019). Although Thompson also overestimates graupel, the results are much closer to observations than the other microphysics parameterization. Regarding rainwater, except for that of WDM6, the profiles are similar, showing small overestimation below 3 km and underestimation above that level. WDM6 overestimates almost the entire profile.

From the DA point of view, the overestimation of snow and graupel by the Thompson and Morrison microphysics parameterizations, respectively, triggers a balance problem between dynamical and microphysical fields in the analysis. The greater the innovation of the microphysics variables is, the greater is the negative impact on the analysis balance when applying the 3DVAR DA. The results shown in Fig. 5 for the residual are quite good; however, the average considers only points where radar data are available, which means that in areas not covered by radar the residuals remain large and affect the forecast started from that analysis. Therefore, because of this heterogeneous reduction in the residuals, the balance of the analysis is affected.

Figures 6 and 7 show the innovations, increments, and residuals of snow and graupel for each microphysical parameterization

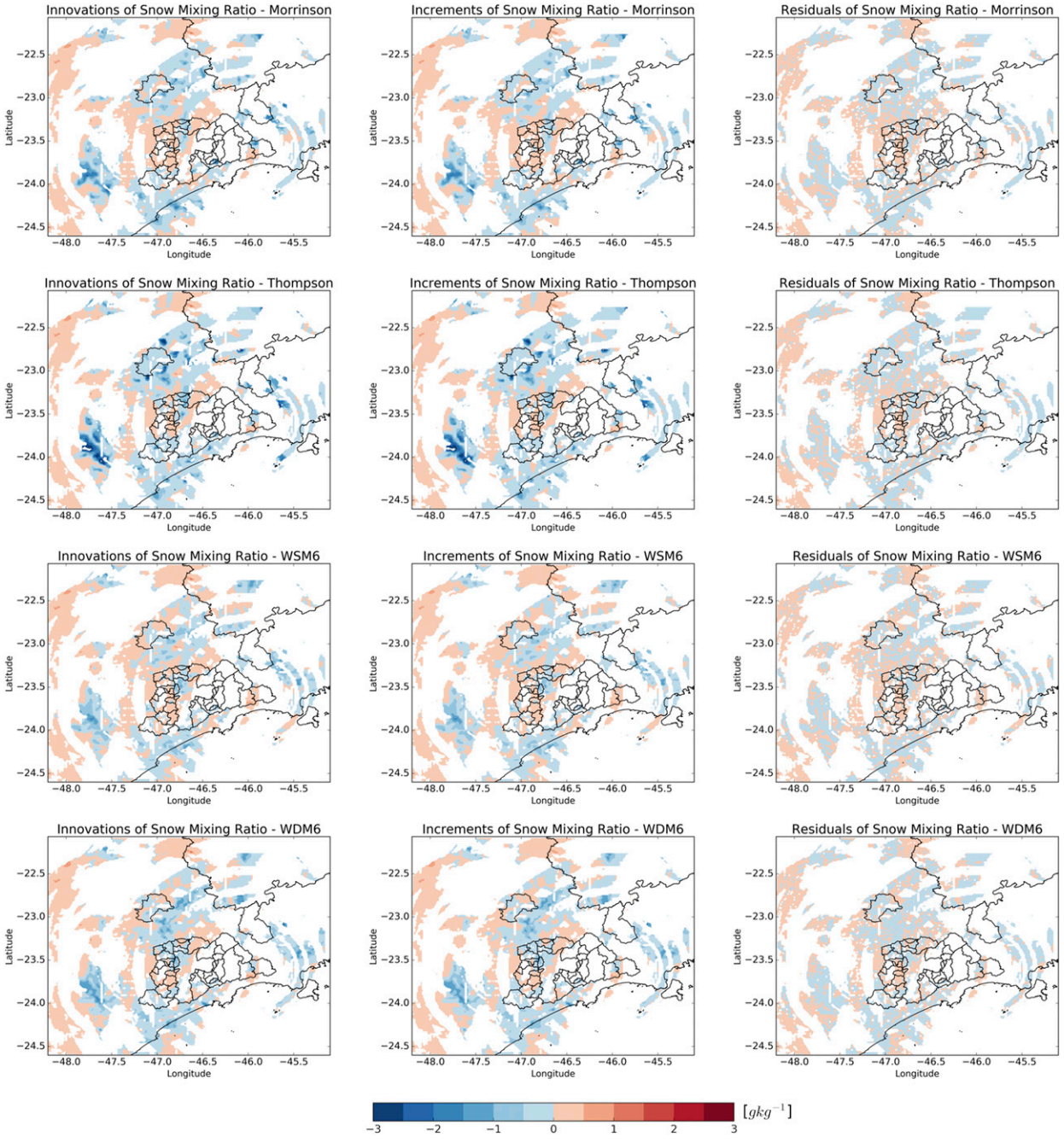

FIG. 6. (left) Increments, (center) innovations, and (right) residuals of snow at the 8-km level for the case of 3 Dec 2016. From the top are the results for Morrinson, Thompson, WSM6, and WDM6.

for the case of 3 December 2016, respectively. Graupel and snow are overestimated by Morrison and Thompson microphysics, respectively. The residuals are very small, which implies that the DA process helps to reduce the misfit between the model and the observations. However, there is a large area with no radar data, where the DA could not correct the aforementioned overestimation. Therefore, although the ability of the DA to correct the microphysics concentrations clearly does not depend on the microphysics scheme, it is still important to choose a proper parameterization to obtain an accurate forecast.

c. *Sensitivity to microphysics parameterization*

In this section, the forecast skills of the four microphysics schemes are evaluated for the five cases. Figure 8 shows the FSS, RMSE, FAR, and POD of the average among all five

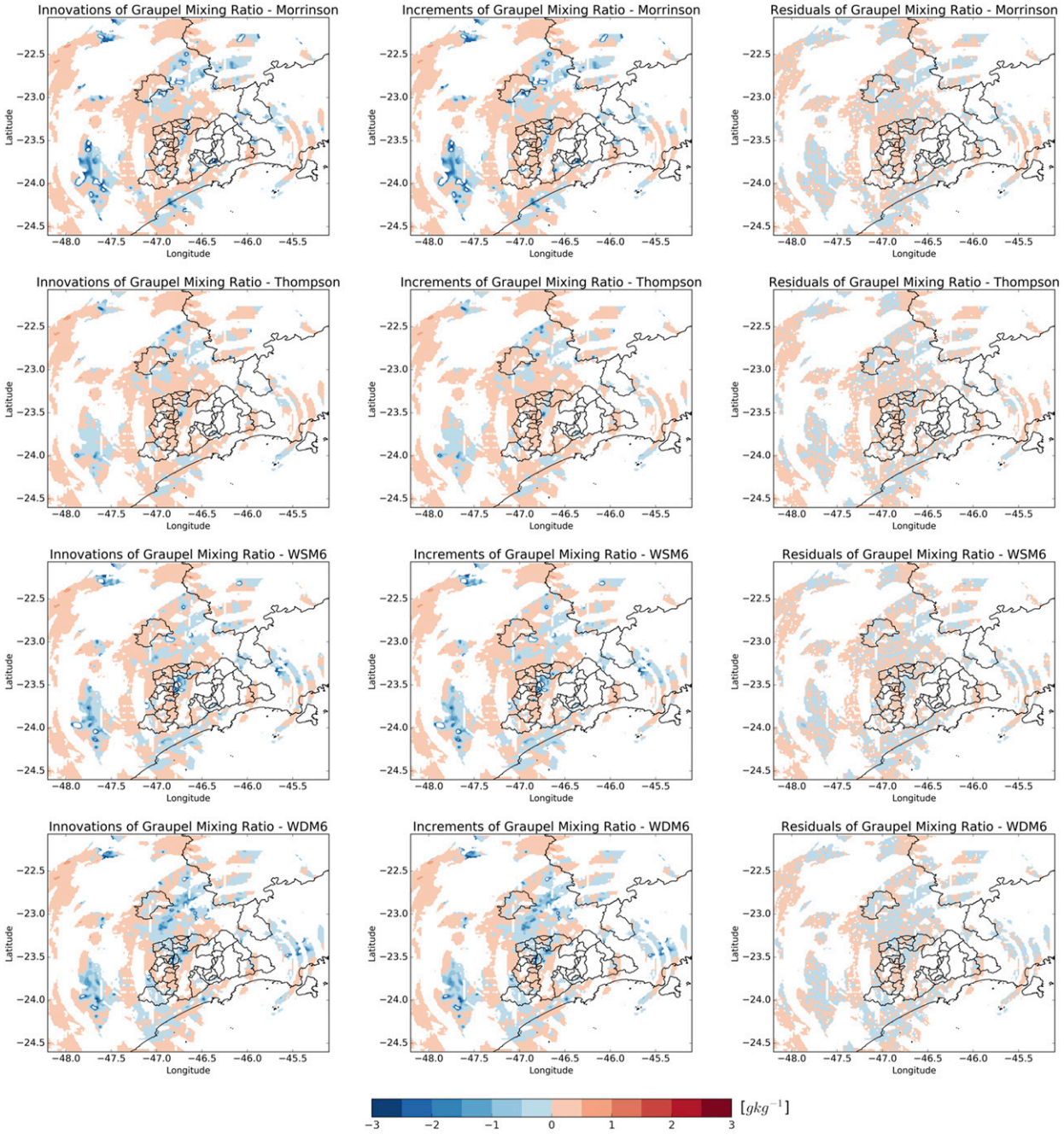

FIG. 7. As in Fig. 6, but for graupel.

cases and all DA methods (including no DA) for each microphysics parameterization employed. The FSS clearly highlights the better performance of the Thompson parameterization during the entire forecast. Additionally, simulations using the Thompson microphysics present the lowest RMSE for all forecast times, followed by simulations using the Morrison scheme. WDM6 has the highest overestimation among all the microphysics. The Thompson scheme has the lowest FAR and similar POD relative to the others, presenting a higher POD between 1 and 3 h of leading time.

Figure 9 shows the 90-min forecasts of composite reflectivity for the case of 27 October 2017. Simulations using the Thompson scheme better depict the convective areas, while the other microphysics tend to overestimate the reflectivity values. Additionally, the shapes of areas with reflectivity higher than 35 dBZ (indicated by yellow areas in Fig. 9) fit better with radar reflectivity than the other microphysics, which have much

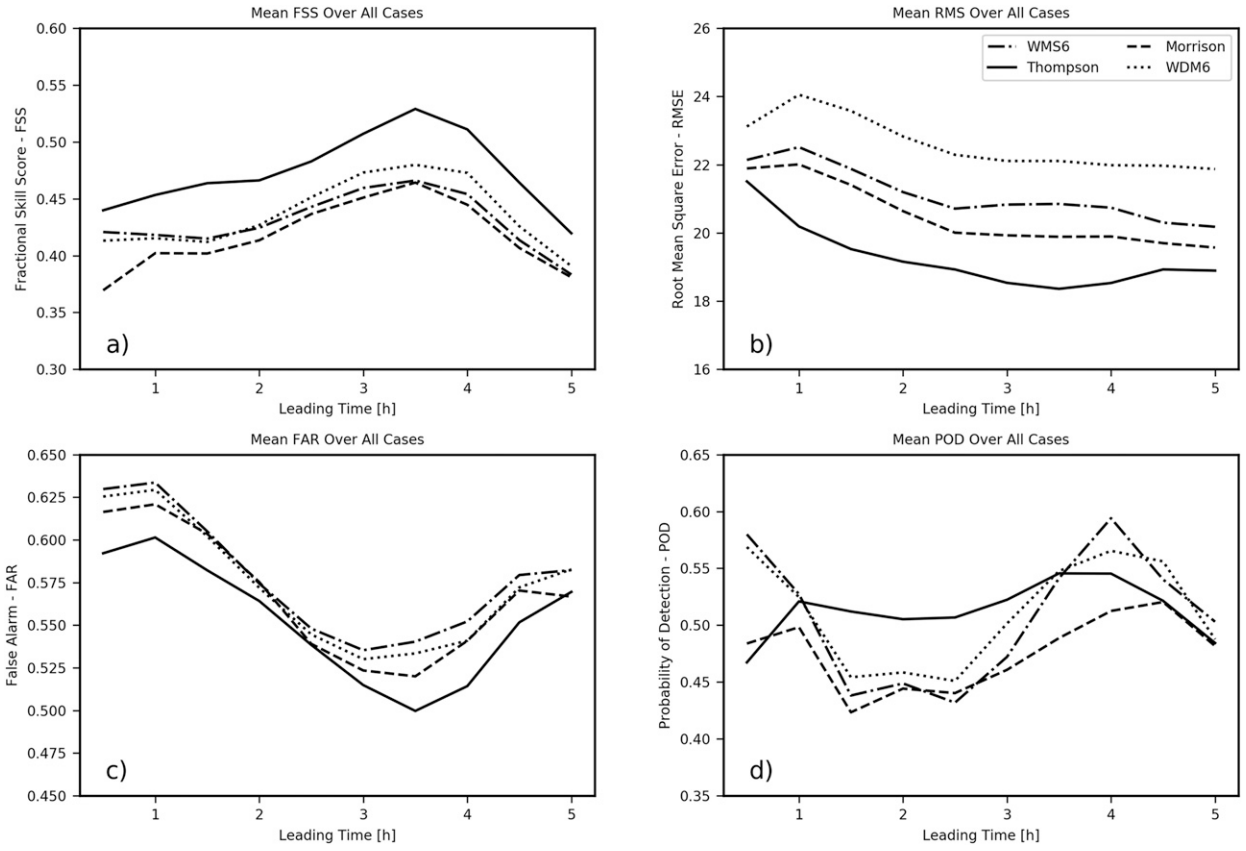

FIG. 8. Temporal evolution of mean (a) FSS, (b) RMS, (c) FAR, and (d) POD over the five cases and the three types of experiments described in Table 3 for each microphysics parameterization.

broader 35-dBZ areas than the observation. Figure 10 highlights the better performance of Thompson for higher reflectivity threshold. For thresholds above 40 dBZ, the skill decreases abruptly in all experiments, except the one with Thompson. The higher forecast skill using Thompson is probably related to the smaller bias in graupel concentrations (see Fig. 5), since graupel and rainwater play a more important role in short-term intense precipitation forecast due to their larger fall speed. A negative characteristic of the Thompson microphysics is that the size of the stratiform area is overestimated. Due to the overall better performance of the Thompson parameterization, in this study, we used this parameterization in the sensitivity experiments of the different DA methods.

d. Sensitivity to radar DA options

This section presents the statistical verifications for the different DA options, as shown in Table 4. Figure 11 shows the statistics for the 14 experiments from Table 4.

The first result from Fig. 11 is that the null-echo assimilation has a notable impact only if DA cycles are performed. Note that the experiments nCYyDA1OLyNE and nCYyDA2OLyNE (dark green and red dotted lines with markers) are very similar to nCYyDA1OLnNE and nCYyDA2OLnNE (dark green and red solid lines), respectively. Additionally, experiments nCYnDA and yCYnDA60M have considerable differences, mainly at the beginning, which means that only by applying cycles the forecast of the reflectivity field is improved. However, up to 2 h of leading time, the FSS shows that experiment yCYnDA60M is still worse than all other experiments with DA. The better performance of the yCYnDA60M experiment is due to the production of hydrometeor species during the cycles; then, at the analysis time, the microphysics of the atmosphere is more realistic than that from experiment nCYnDA.

All experiments without cycles (nCY) tend to have low POD during the entire forecast and relatively high FSS at the beginning, even though the FSS decreases during the forecast. Without cycles, the background comes from GFS, and the hydrometeors are all set to zero. Then, the analysis tends to be closer to observation than those that come from the cycles. However, because the hydrometeors have no dynamic support, the accuracy drops quickly during the forecast in comparison to the simulations with cycles.

Another remarkable result from Fig. 11 is that the experiment yCYyDA60M1OLyNE (light blue dotted line) has the best result regarding FAR, FSS, and RMSE. However, its POD is much lower than those without null-echo assimilation. The null-echo assimilation reduces reflectivity in general by removing spurious convection. This leads to less frequent reflectivity values over the selected threshold and then reduces

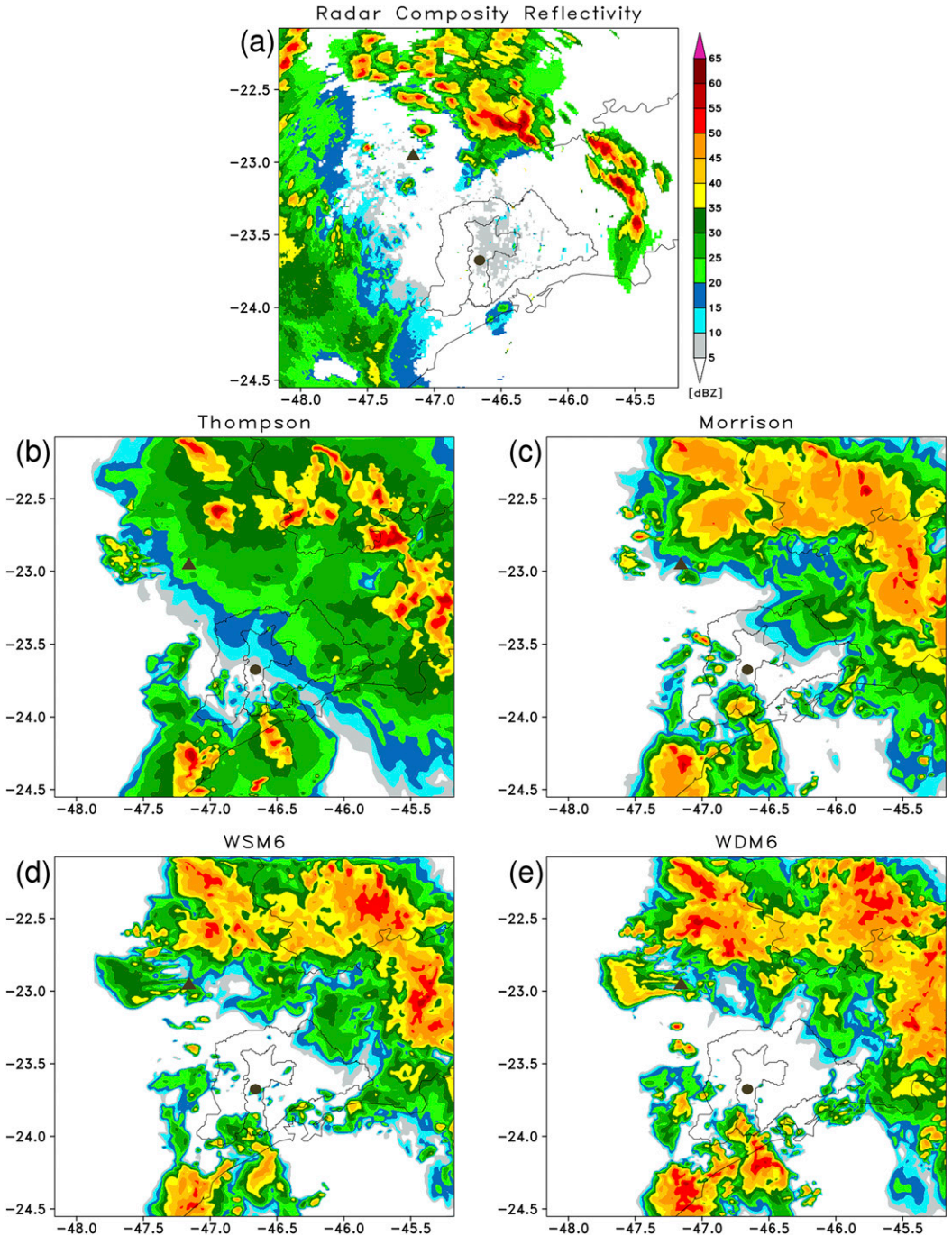

FIG. 9. Composite reflectivity of experiment yCYyDA for the case of 27 Oct for each microphysics parameterization: (b) Thompson, (c) Morrison, (d) WSM6, and (e) WDM6. (a) The radar observation is also shown.

hits that occur by chance (i.e., cells that are misplaced in the analysis but can lead to a correct detection in the forecast). Therefore, it is expected that even if only spurious echoes are removed, POD decreases and it is not necessarily due to degradation of the forecast. Nevertheless, the null-echo assimilation may also remove part of the real convection, mainly the growing cells, still not visible by the radar due to its initial stage.

Figure 11 gives an overview of the averaged results over the five cases and indicates that the worst and the best experiments are nCYnDA and yCYyDA60M1OLyNE, respectively. To perform a deeper analysis in the individual contribution of each case to the average, Fig. 12 shows the statistical indices for the five cases and experiments nCYnDA and yCYyDA60M1OLyNE. FSS (Fig. 12a) indicates that all

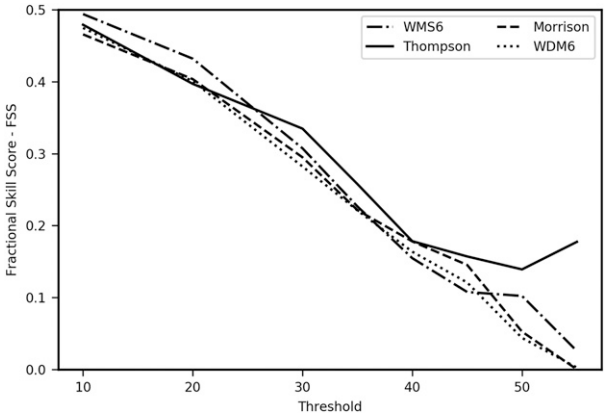

FIG. 10. Fractional skill score for different thresholds from experiment yCYyDA for the case of 27 Oct 2017.

cases have improved after performing DA, however, different behaviors are observed. For cases 1 (3 December 2016—black lines) and 3 (6 March 2017—red lines), the initial improvements are larger and they last for approximately 4 and 3 h, respectively. For case 5 (27 October 2017—blue lines), the improvement also lasts for approximately 3 h, but the magnitude is smaller at the beginning compared to the aforementioned cases. For cases 2 (2 February 2017—cyan lines) and 4 (5 May 2017—orange lines), the improvements last for the entire forecast. The local isolated character of the storms in case 2 (under weak synoptic forcing) may explain its longer lasting positive impact of DA. The case 4 is a peculiar one because the QLCS formed in the west part of the domain d03 at 2100 UTC (Fig. 2). During the cycle between 1500 and 1800 UTC the system was almost entirely outside of the domain and only isolated storms were present, which may be the reason for similarities with case 2. The other indices also show that the experiment with radar DA improved the forecast in all five cases. Case 1 has the best forecasts among all five cases, with the highest FSS and POD and the lowest FAR and RMSE (up to 2 h). Conversely, cases 2 and 4 share the worst performances.

The analysis is now divided into the three main features of the experiments described in Table 4: (i) the benefits of doing a DA cycle before producing the final analysis; (ii) the benefit of doing two outer loops in the minimization instead of only one; and (iii) the impact of applying the null-echo capability of WRFDA.

Figure 13 shows the average statistics obtained by grouping the eight experiments (only with cycles and DA—yCYyDA) from Table 4 into three classes: (i) cycles of 30 and 60 min; (ii) 1 and 2 outer loops; and (iii) with and without null-echo assimilation. The three features impact the forecasts. The increase in

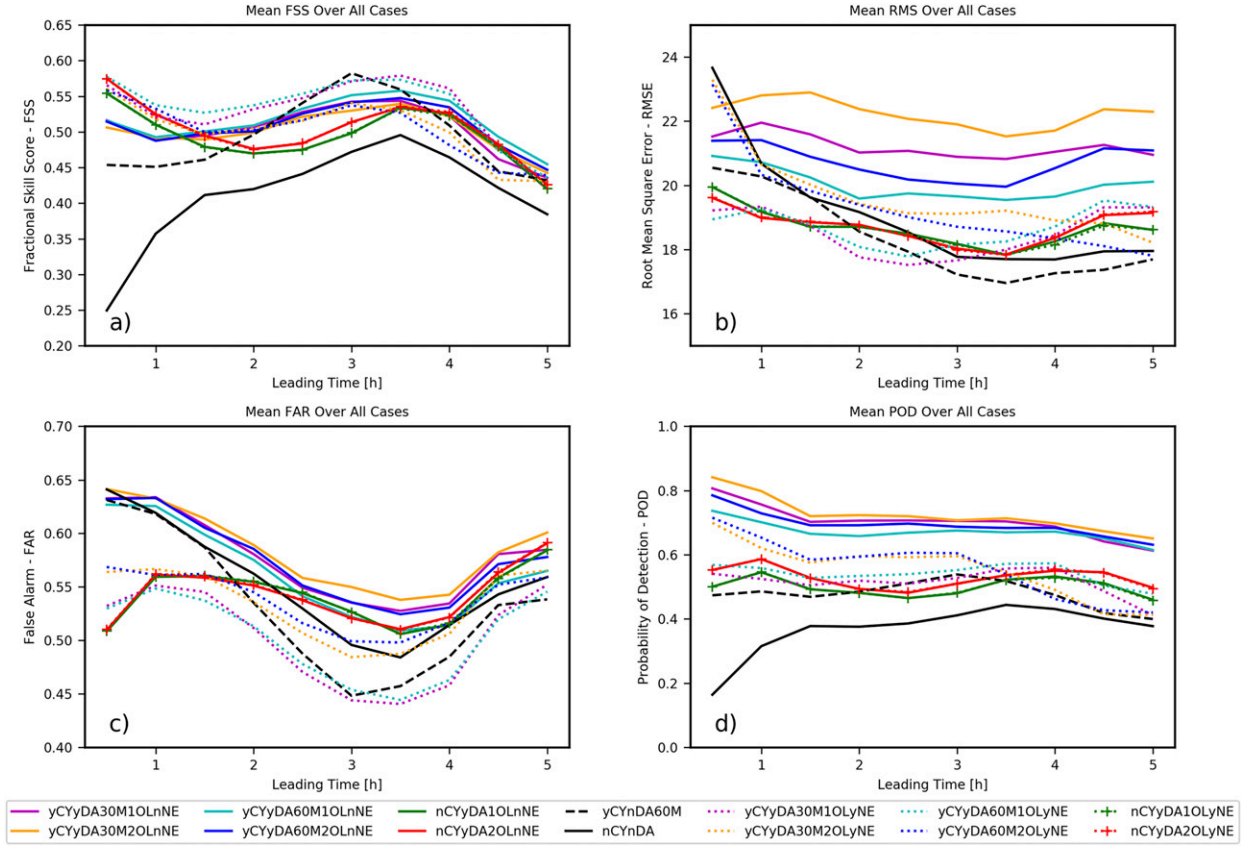

FIG. 11. Temporal evolution of the mean (a) FSS, (b) RMS, (c) FAR, and (d) POD over the five cases for each experiment in Table 4.

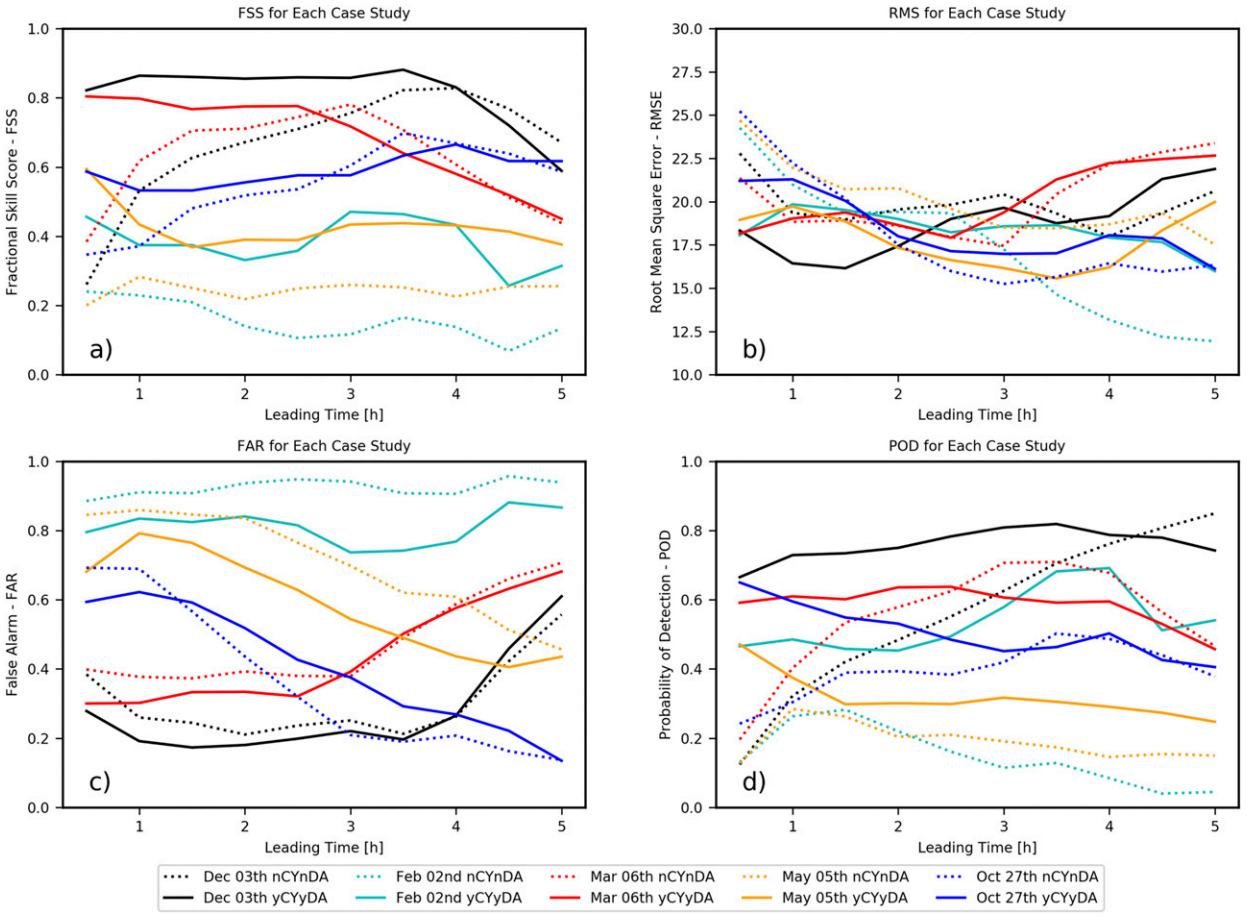

FIG. 12. Temporal evolution of (a) FSS, (b) RMS, (c) FAR, and (d) POD for the five cases (indicated by different colors) for the experiments nCYnDA (dotted lines) and yCYyDA60M1OLnNE (solid lines).

the frequency of assimilation during the cycle shows the smallest impact. The overall result indicates that increasing the frequency from 60 to 30 min increases the POD as well as FAR. The FSS and RMSE are worse when the 30-min cycle is applied. The results deteriorate despite the assimilation of more radar data, which is probably because more noise is being introduced in the system in each cycle and the already known noise/unbalance introduced by the 3DVAR radar DA (Vendrasco et al. 2016) is greater when a 30-min cycle is used. The use of two outer loops results in a similar behavior to the 30-min cycle. The use of two outer loops increases the POD, but the areas of spurious convection also become larger, which results in a higher FAR, higher RMSE and lower FSS. Finally, to alleviate this spurious convection, the null-echo assimilation seems to be very useful, since it has a relatively large positive impact by increasing FSS and reducing RMSE and FAR. However, null-echo assimilation also reduces the POD, which may be due to the reduction of hits that occur by chance, as explained before, and/or by removing real convection at the early stage.

Figure 14 shows the observed and simulated composite reflectivity for the 6 March 2017 case as an example of the role of DA cycles and null-echo assimilation in improving the representation of convective and stratiform areas. The fields inside the purple rectangle in Fig. 14 are those from experiments nCYnDA, nCYyDA1OLnNE, and nCYyDA2OLyNE. In general, the forecast without any DA predicts precipitation in some areas but does not capture the pattern observed by radar. The experiments with DA (nCYyDA1OLnNE and nCYyDA2OLyNE) improve the precipitation field in the center of the domain relative to observations, despite the lower intensity. When comparing these experiments and others without cycles, for all the cases (not shown), the use of null-echo assimilation and the extra outer loop has a very small impact when not cycling the DA. This result is expected and can be explained by two reasons: first, since the DA is not cycled, the backgrounds of the hydrometeors are all zero, and after the DA process with one outer loop, the analysis is already very similar to observations (not shown). Therefore, it is not expected that a second outer loop would have a high impact. It is known that the outer loop improves the linearization of **H** near the minimum of the cost function, thus improving the computation of the gradient and producing a solution that is closer to the actual minimum. However, due to the use of the indirect assimilation of reflectivity and the absence of the cycles, the cumulative impact of the outer loop is minimized.

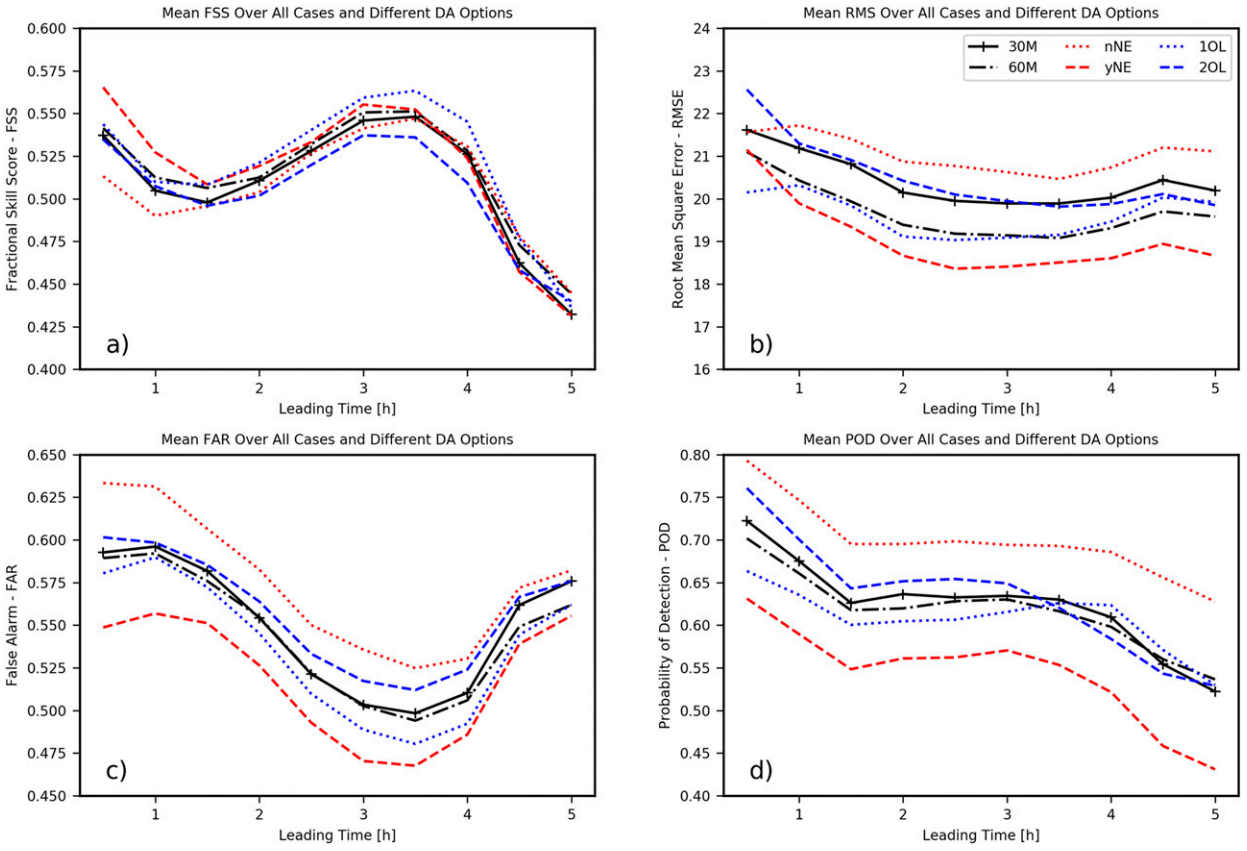

FIG. 13. Temporal evolution of mean (a) FSS, (b) RMS, (c) FAR, and (d) POD over the five cases for all experiments with cycles and data assimilation (yCyDA) in Table 4. The experiments were also averaged considering those with cycles of 30 and 60 min, with 1 and 2 outer loops, and with and without null-echo assimilation.

Second, the objective of the null-echo assimilation is the removal of spurious convection, and since there is no convection at the analysis time when not cycling, the null-echo assimilation should not have effect. In this case, the small differences between the experiments nCYyDA1OLnNE and nCYyDA2OLyNE rely only on the number of outer loops.

The most evident difference observed in Fig. 14 is the overestimation in simulations inside the red square (i.e., in the experiments with cycles and the null-echo assimilation turned off). Additionally, it is clear that the null-echo assimilation reduces spurious convection and improves the forecast (black square in Fig. 14). The null echo also eliminates real precipitation in some areas, such as the easternmost region of the domain over the continent. The null-echo assimilation option of WRFDA uses the radar reflectivity to decide whether the precipitation from WRF is spurious, but the problem is that radar observes precipitation (rain drops) but not clouds droplets. If the model produces precipitation a few minutes before it truly occurs, the null-echo tool would remove this feature, and the model would not be able to predict it; an example of this behavior can be seen in Fig. 15.

The purple circles and arrow in Fig. 15a show regions where the NE reduced the reflectivity factor (negative values), and Fig. 15b shows that no reflectivity is observed in those regions at analysis time (1800 UTC); however, after 30 min (Fig. 15c) intense convection is observed in the southmost purple circle region and, also, developing convection is shown in the northmost purple circle region. Intense convection is observed in that area in later times (not shown). These two regions are examples of the negative effect of NE mentioned above, while the purple arrow points to an area where NE really removed spurious convection.

e. *Masked null-echo assimilation*

Because the null-echo assimilation can remove potential convective clouds before the rain droplets are large enough to be detected by the radar, as explained in the previous section, a new methodology was implemented employing satellite data to create a convective cloud mask (CCM) to be employed during the assimilation process. According to Machado and Rossow (1993), convective clouds in the tropics can be identified by selecting satellite image pixels containing infrared brightness temperature (BT_{IR}) lower than 245 K. However, since we are looking for convective clouds in the early development stage, a warmer threshold of 253 K was employed. Therefore, a mask of BT_{IR} was created using data from the *GOES-13* satellite, and the null-echo assimilation was applied only when $BT_{IR} >$ 253 K. The new experiment was performed for all case studies

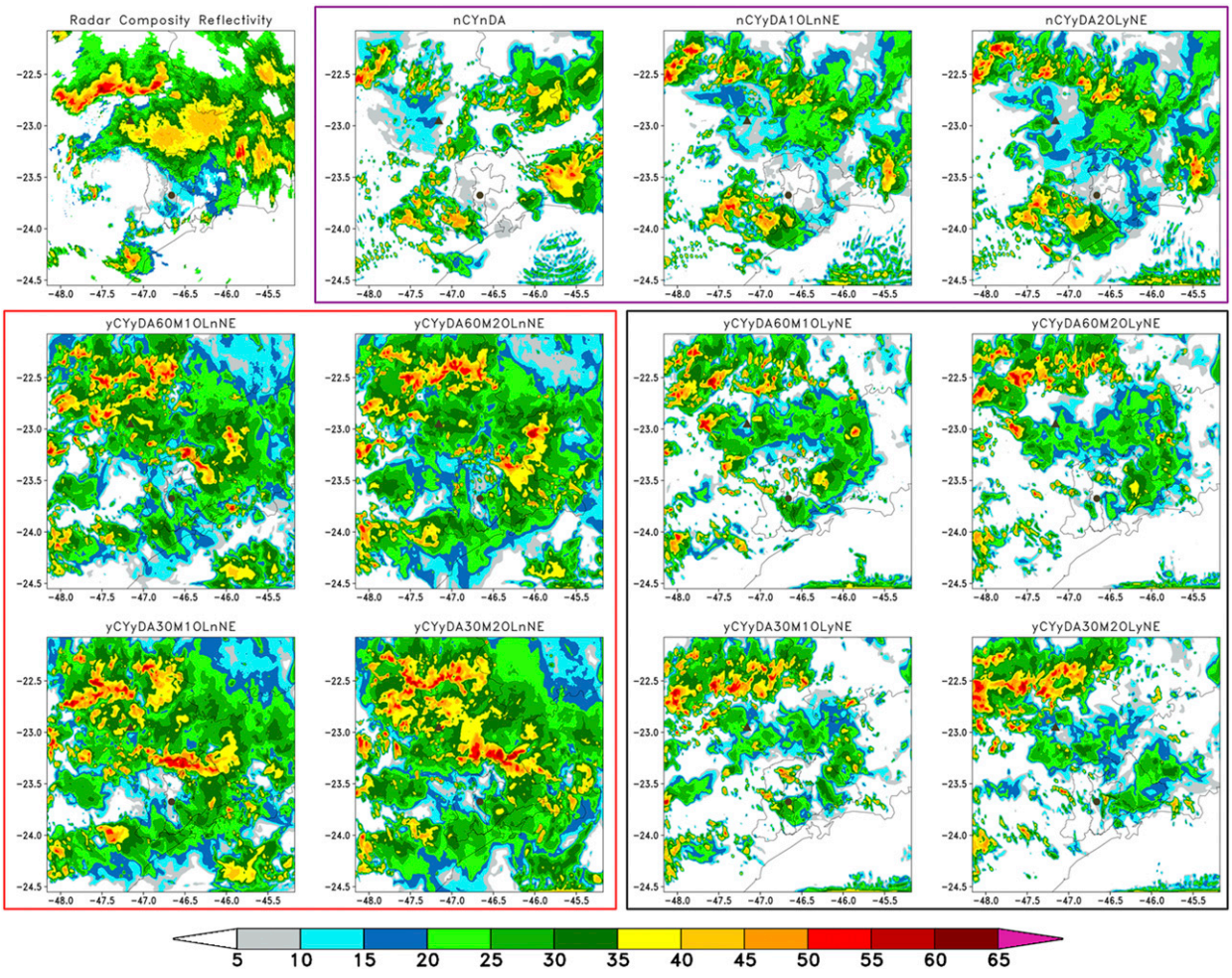

FIG. 14. Composite reflectivity (dBZ) at 1930 UTC 6 Mar 2017 from radar (shown at the top-left corner) and different experiments with WRF. The results from WRF are grouped as follows: without cycles (inside purple rectangle), with cycles and without null-echo (red square), and with cycles and with null-echo (black square). Inside the purple rectangle from left to right are the experiments nCYnDA, nCYyDA1OLnNE, and nCYyDA2OLyNE. Inside the red and black squares, in the left column are the 1 outer loop experiments, 2 outer loops are on the right side, 60 min are on the top, and 30 min are on the bottom.

using the same configuration of experiment yCYyDA60MOL1yNE, which produced the best result among all the experiments listed in Table 4.

The benefits of applying the CCM vary according to the different cases. For cases 1, 2, and 3 the implementation of the CCM improved the forecasts, but the same was not observed for cases 4 and 5 (Fig. 16). The average of cases 1, 2, and 3 shows higher FSS and POD and lower RMSE when using the CCM. The FAR is slightly higher up to a 2-h forecast and then nearly the same. Conversely, the average of cases 4 and 5 shows slightly lower FSS and higher RMSE and FAR when using the CCM. The POD is also higher for experiments employing the CCM. It occurs because the CCM reduces the area where the null-echo assimilation is applied and, for these cases, it is producing overestimation of stratiform precipitation, and more hits are being counted, which increases the POD index.

The different forecasting skills when using the CCM among the cases might be related to the cloud types present over the domain. For cases 4 and 5, it was observed in the east side of the convective cells a band of thick cirrus clouds, while in case 1, despite the similar pattern of cloudiness, there were no thick cirrus clouds. Case 2 was characterized by convective cells surrounded by clear sky mixed with scattered lower level cloud tops and few cirrus. In case 3, the convective clouds were surrounded by low, medium, and high clouds, but they were not enough to compromise the CCM. These evidences suggest that the high clouds associated with the eastern cloud band in cases 4 and 5 compromised the convective cloud mask, preventing null-echo observations from being assimilated.

The performance of experiments with the CCM for the average of cases 4 and 5 is mainly due to the errors in case 5. The larger error in case 5 is mostly due to the overestimation of stratiform precipitation; however, intense convective storms were better depicted (not shown). Figure 17 shows higher FSS for higher thresholds when applying the CCM for case 5, in particular for thresholds greater than 20 dBZ. The FSS of the

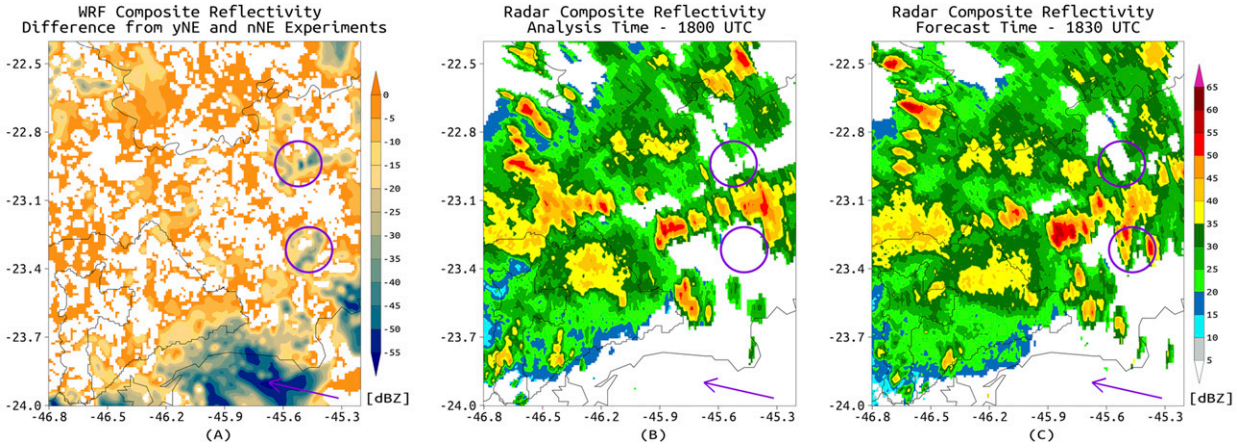

FIG. 15. (a) Difference of composite reflectivity from experiments yCYyDA60M1OLyNE and yCYyDA60M1OLnNE for the case of 1800 UTC 6 Mar 2017 and the radar reflectivity composite at (b) 1800 UTC and (c) 1830 UTC. Purple circles and arrow show areas with great impact of null-echo assimilation.

experiment without CCM decreases more rapidly for thresholds above 20 dB*Z*.

Overall, the use of the CCM improved the quality of the short-term forecast of intense storms since it allowed some convective systems to develop to their mature stage instead of suppressing them at their initial stage. However, in some cases the negative feedback is the overestimation of the stratiform precipitation, which led to the lower skill observed in the statistical indices. Therefore, we believe that the use of the mask when applying the null-echo assimilation should be considered;

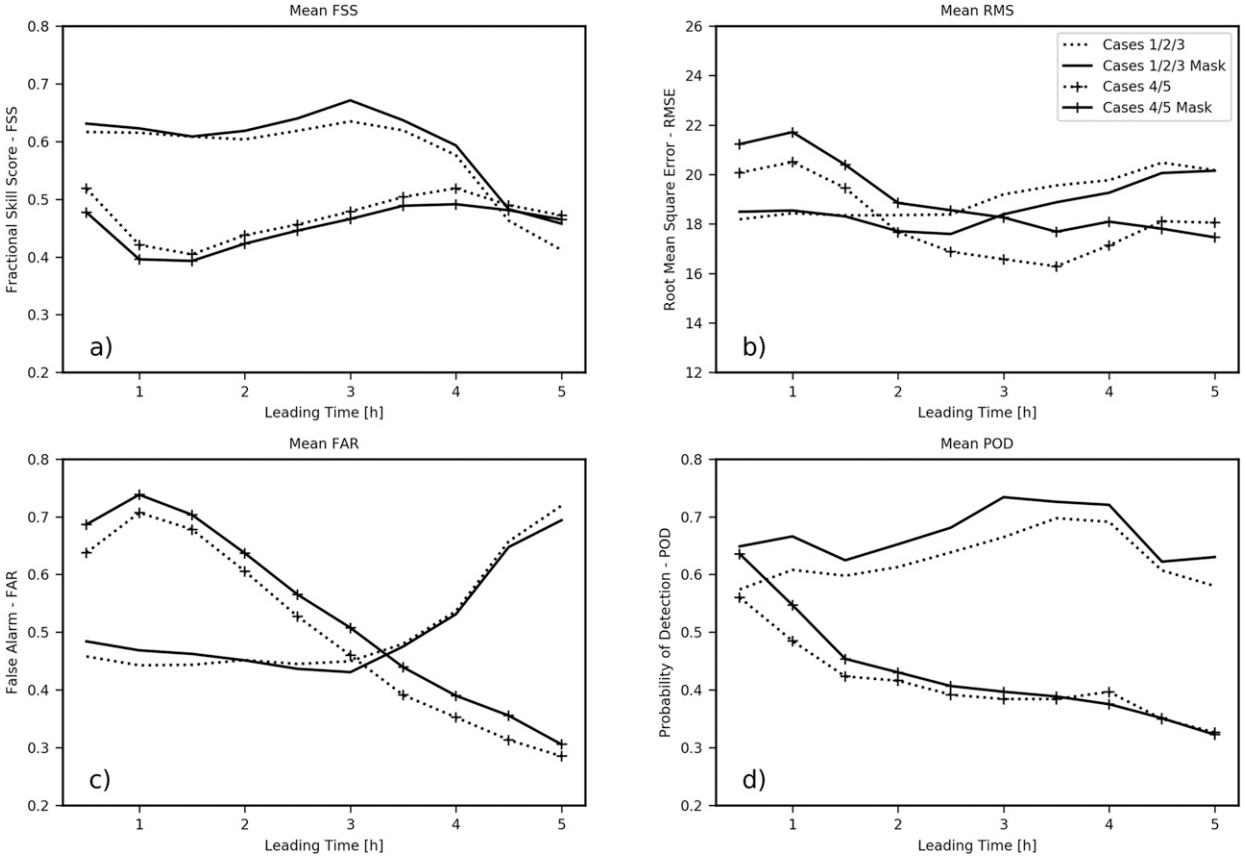

FIG. 16. Temporal evolution of mean (a) FSS, (b) RMS, (c) FAR, and (d) POD over cases 1, 2, and 3 (dotted and solid lines) and cases 4 and 5 (dotted and solid lines with markers). Dotted (solid) lines are for experiments without (with) convective cloud mask.

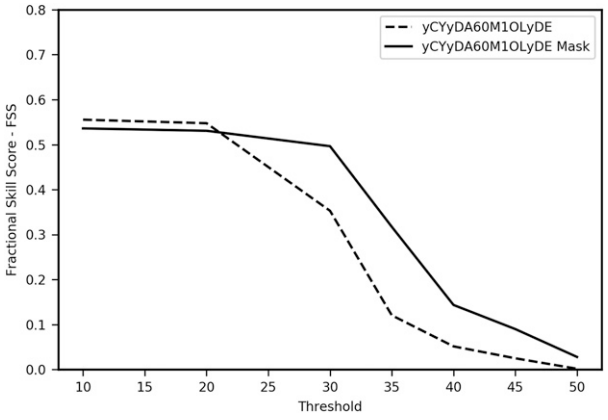

FIG. 17. Fractional skill score for different thresholds from experiment yCYyDA60M1OLyNE with and without the convective cloud mask for the case of 27 Oct 2017.

however, more cases have to be evaluated. The use of more complex convective cloud mask employing normalized area expansion (Machado and Laurent 2004), Lagrangian brightness temperature time derivation, cloud classifications or other products derived from satellites, could positively impact the forecast and should be evaluated in the future with the new *GOES-16*/Advanced Baseline Imager (ABI) imagery and derived products.

4. Conclusions

This study evaluates the potential benefits of radar reflectivity and radial velocity DA for short-term convective storms forecasting using the WRF's 3DVAR system. Five cases with convective storms in southeastern Brazil were selected and statistical indices were calculated to assess the accuracy of the model in predicting reflectivity for up to 6 h. The framework tested here is able to forecast heavy precipitation with acceptable accuracy and can be used for operational purposes.

Initially, experiments were conducted to verify the microphysics parameterizations that better reproduce the reflectivity field observed by radar. The Thompson microphysics parameterization produced the reflectivity fields that best corresponded to observations. The areas of convective precipitation were better depicted by Thompson microphysics, while the stratiform area coverage was overestimated. The overestimation is related to the overproduction of snow by this scheme, as shown in section 3b. This kind of information is very relevant when running a nowcasting framework to forecast severe convective systems. In this case, it is more important to better predict the areas with intense precipitation and keep larger errors in the stratiform regions. However, these errors cannot be too large because the overprediction of stratiform areas can lead to an increase in the atmosphere stabilization and then to affect the development of convection.

It should be advised that the observational operator can take full advantage of double moment microphysics (e.g., Morrison and WDM6 schemes) only if changes in the total number concentrations are considered. Otherwise, the impact of using a double moment scheme on the analysis will rely only on the model integration between cycles. Moreover, although the advantages of assimilating retrievals regarding the aforementioned nonlinearities issues, it does not take into account changes in the particle size distribution, which may affect the results.

In the second part of the paper, the impact of increasing the frequency of the assimilation cycles from 60- to 30-min intervals was analyzed. According to the schematic diagram of the cycling strategy shown in Fig. 3, the 60-min cycle represents four DA cycles, while the 30-min cycle represents seven. In the latter option, much more data are assimilated, which results in lower accuracy in the precipitation forecast. This result is likely because the model does not have enough time (only 30 min) to balance the analysis before the next assimilation, and the noise in the final analysis is greater than that when a 60-min cycle is employed. There are some options that could alleviate this noise problem, such as digital filters (Lynch 1993) and the large-scale analysis constraint (LSAC; Vendrasco et al. 2016), but this study intended to evaluate 30- and 60-min cycles without any of these artifacts. Another DA option tested was the use of more outer loops, and the results indicated better accuracy when only one outer loop was applied. The benefits of the additional outer loop are very small if no relevant amount of data are added in the loop, and the noise in the analysis can increase. Because the amount of rejected radar data was small in the first loop, the second loop should be avoided.

The null-echo assimilation was the most effective strategy in improving the precipitation forecast. Radar DA tends to cause an overestimation of precipitation, and the null-echo assimilation alleviates this problem by removing spurious convection. The best result was achieved when radar DA employed a 60-min cycle and the null-echoes were assimilated. Despite the good performance of the null-echo assimilation, this technique also removed some real convection before its development (i.e., when no precipitation had been observed yet by the radar).

A convective cloud mask was implemented using the satellite infrared brightness temperature to mitigate the aforementioned problem with null-echo assimilation, and the results were positive in most of the cases. The experiment using this mask was able to improve the forecast, but not in the entire domain and in all cases, and further investigation must be done. For intense convection, however, the skill was better in all cases. New techniques to design the convective cloud mask should be studied. The 16 channels and the high temporal and spatial resolutions of *GOES-16* allow the development of more complex and effective CCMs.

Acknowledgments. The authors acknowledge Fapesp Grant 2015/14497-0 for funding this research and the Department of Airspace Control (DECEA) and the Hydraulic Technology Center (CTH) for providing the radar data.

REFERENCES

Aksoy, A., D. C. Dowell, and C. Snyder, 2009: A multicase comparative assessment of the ensemble Kalman filter for assimilation of radar observations. Part I: Storm-scale analyses. *Mon. Wea. Rev.*, **137**, 1805–1824, https://doi.org/10.1175/2008MWR2691.1.

Bao, J., S. A. Michelson, and E. D. Grell, 2019: Microphysical process comparison of three microphysics parameterization schemes in the WRF Model for an idealized squall-line case study. *Mon. Wea. Rev.*, **147**, 3093–3120, https://doi.org/10.1175/MWR-D-18-0249.1.

Barker, D. M., W. Huang, Y. R. Guo, A. J. Bourgeois, and Q. N. Xiao, 2004: A three-dimensional variational data assimilation system for MM5: Implementation and initial results. *Mon. Wea. Rev.*, **132**, 897–914, https://doi.org/10.1175/1520-0493(2004)132<0897:ATVDAS>2.0.CO;2.

Berg, L. K., W. I. Gustafson, E. I. Kassianov, and L. Deng, 2013: Evaluation of a modified scheme for shallow convection: Implementation of CuP and case studies. *Mon. Wea. Rev.*, **141**, 134–147, https://doi.org/10.1175/MWR-D-12-00136.1.

Carlin, J. T., J. Gao, J. C. Snyder, and A. V. Ryzhkov, 2017: Assimilation of ZDR columns for improving the spinup and forecast of convective storms in storm-scale models: Proof-of-concept experiments. *Mon. Wea. Rev.*, **145**, 5033–5057, https://doi.org/10.1175/MWR-D-17-0103.1.

Cheng, R., R. Yu, Y. Fu, and Y. Xu, 2011: Impact of cloud microphysical processes on the simulation of Typhoon Rananim near shore. Part I: Cloud structure and precipitation features. *Acta Meteor. Sin.*, **25**, 441–455, https://doi.org/10.1007/s13351-011-0405-0.

Courtier, P., J. N. Thépaut, and A. Hollingsworth, 1994: A strategy for operational implementation of 4D-Var, using an incremental approach. *Quart. J. Roy. Meteor. Soc.*, **120**, 1367–1387, https://doi.org/10.1002/qj.49712051912.

——, and Coauthors, 1998: The ECMWF implementation of three-dimensional variational assimilation (3D-Var). I: Formulation. *Quart. J. Roy. Meteor. Soc.*, **124**, 1783–1807, https://doi.org/10.1002/qj.49712455002.

Ferrier, B. S., Y. Jin, Y. Lin, T. Black, E. Rogers, and G. DiMego, 2002: Implementation of a new grid-scale cloud and precipitation scheme in the NCEP Eta model. *19th Conf. on Weather Analysis and Forecasting/15th Conf. on Numerical Weather Prediction*, San Antonio, TX, Amer. Meteor. Soc., 10.1, https://ams.confex.com/ams/SLS_WAF_NWP/techprogram/paper_47241.htm .

Fovell, R. G., K. L. Corbosiero, and H. Kuo, 2009: Cloud microphysics impact on hurricane track as revealed in idealized experiments. *J. Atmos. Sci.*, **66**, 1764–1778, https://doi.org/10.1175/2008JAS2874.1.

Gao, J., and D. J. Stensrud, 2012: Assimilation of reflectivity data in a convective-scale, cycled 3DVAR framework with hydrometeor classification. *J. Atmos. Sci.*, **69**, 1054–1065, https://doi.org/10.1175/JAS-D-11-0162.1.

——, M. Xue, K. Brewster, and K. K. Droegemeier, 2004: A three-dimensional variational data analysis method with recursive filter for Doppler radars. *J. Atmos. Oceanic Technol.*, **21**, 457–469, https://doi.org/10.1175/1520-0426(2004)021<0457:ATVDAM>2.0.CO;2.

Grabowski, W. W., 2014: Extracting microphysical impacts in large-eddy simulations of shallow convection. *J. Atmos. Sci.*, **71**, 4493–4499, https://doi.org/10.1175/JAS-D-14-0231.1.

Helmus, J. J., and S. M. Collis, 2016: The Python ARM Radar Toolkit (Py-ART), a library for working with weather radar data in the Python programming language. *J. Open Res. Software*, **4**, e25, https://doi.org/10.5334/jors.119.

Hong, S., and J. J. Lim, 2006: The WRF single-moment 6-class microphysics scheme (WSM6). *J. Korean Meteor. Soc.*, **42**, 129–151.

——, Y. Noh, and J. Dudhia, 2006: A new vertical diffusion package with an explicit treatment of entrainment processes. *Mon. Wea. Rev.*, **134**, 2318–2341, https://doi.org/10.1175/MWR3199.1.

Hsiao, L., D. Chen, Y. Kuo, Y. Guo, T. Yeh, J. Hong, C. Fong, and C. Lee, 2012: Application of WRF 3DVAR to operational typhoon prediction in Taiwan: Impact of outer loop and partial cycling approaches. *Wea. Forecasting*, **27**, 1249–1263, https://doi.org/10.1175/WAF-D-11-00131.1.

Iacono, M. J., J. S. Delamere, E. J. Mlawer, M. W. Shephard, S. A. Clough, and W. D. Collins, 2008: Radiative forcing by long-lived greenhouse gases: Calculations with the AER radiative transfer models. *J. Geophys. Res.*, **113**, D13103, https://doi.org/10.1029/2008JD009944.

Illari, L., 1987: The spin-up problem. ECMWF Tech. Memo. 137, 33 pp., https://doi.org/10.21957/ucq8y9b3c.

James, C., and R. Houze Jr., 2001: A real-time four-dimensional Doppler dealiasing scheme. *J. Atmos. Oceanic Technol.*, **18**, 1674–1683, https://doi.org/10.1175/1520-0426(2001)018<1674:ARTFDD>2.0.CO;2.

Kawabata, T., T. Schwitalla, A. Adachi, H. S. Bauer, V. Wulfmeyer, N. Nagumo, and H. Yamauchi, 2018: Observational operators for dual polarimetric radars in variational data assimilation systems (PolRad VAR v1.0). *Geosci. Model Dev.*, **11**, 2493–2501, https://doi.org/10.5194/gmd-11-2493-2018.

Kong, R., M. Xue, and C. Liu, 2018: Development of a hybrid En3DVar data assimilation system and comparisons with 3DVar and EnKF for radar data assimilation with observing system simulation experiments. *Mon. Wea. Rev.*, **146**, 175–198, https://doi.org/10.1175/MWR-D-17-0164.1.

Li, X., J. R. Mecikalski, and D. Posselt, 2017: An ice-phase microphysics forward model and preliminary results of polarimetric radar data assimilation. *Mon. Wea. Rev.*, **145**, 683–708, https://doi.org/10.1175/MWR-D-16-0035.1.

Lim, K. S., and S. Hong, 2010: Development of an effective double-moment cloud microphysics scheme with prognostic cloud condensation nuclei (CCN) for weather and climate models. *Mon. Wea. Rev.*, **138**, 1587–1612, https://doi.org/10.1175/2009MWR2968.1.

Lin, C., S. Vasić, A. Kilambi, B. Turner, and I. Zawadzki, 2005: Precipitation forecast skill of numerical weather prediction models and radar nowcasts. *Geophys. Res. Lett.*, **32**, L14801, https://doi.org/10.1029/2005GL023451.

Lynch, P., 1993: Digital filters for numerical weather prediction. HIRLAM Tech. Rep. 10, 42 pp., http://mathsci.ucd.ie/~plynch/Publications/HIRLAM_Tech_Report_10.pdf.

Machado, L. A. T., and W. B. Rossow, 1993: Structural characteristics and radiative properties of tropical cloud clusters. *Mon. Wea. Rev.*, **121**, 3234–3260, https://doi.org/10.1175/1520-0493(1993)121<3234:SCARPO>2.0.CO;2.

——, and H. Laurent, 2004: The convective system area expansion over Amazonia and its relationships with convective system life duration and high-level wind divergence. *Mon. Wea. Rev.*, **132**, 714–725, https://doi.org/10.1175/1520-0493(2004)132<0714:TCSAEO>2.0.CO;2.

——, and Coauthors, 2014: The CHUVA Project: How does convection vary across Brazil? *Bull. Amer. Meteor. Soc.*, **95**, 1365–1380, https://doi.org/10.1175/BAMS-D-13-00084.1.

Marshall, J. S., and W. M. Palmer, 1948: The distribution of raindrops with size. *J. Meteor.*, **5**, 165–166, https://doi.org/10.1175/1520-0469(1948)005<0165:TDORWS>2.0.CO;2.

Milbrandt, J. A., and M. K. Yau, 2005: A multimoment bulk microphysics parameterization. Part II: A proposed three-moment closure and scheme description. *J. Atmos. Sci.*, **62**, 3065–3081, https://doi.org/10.1175/JAS3535.1.

Min, K.-H., Y. Kim, K. Park, and G. Lee, 2017: Assimilation of null-echo from radar observations for short-term precipitation forecasting. *28th Conf.on Weather Analysis and Forecasting / 24th Conf. on Numerical Weather Prediction*, Seattle, WA, Amer. Meteor. Soc., 1161, https://ams.confex.com/ams/97Annual/webprogram/Paper304184.html.

Ming, C., S. Y. Fan, J. Zhong, X. Y. Huang, Y. R. Guo, W. Wang, Y. Wang, and B. A. Kuo 2009: A WRF-based rapid updating cycling forecast system of BMB and its performance during the summer and Olympic Games 2008. *World Meteorological Organization Symp. on Nowcasting and Very Short Term Forecasting*, Whistler, BC, Canada, WMO, 6 pp., https://citeseerx.ist.psu.edu/viewdoc/download?doi=10.1.1.496.8761&rep=rep1&type=pdf.

Mohan, P. R., C. V. Srinivas, V. Yesubabu, R. Baskaran, and B. Venkatraman, 2019: Tropical cyclone simulations over Bay of Bengal with ARW model: Sensitivity to cloud microphysics schemes. *Atmos. Res.*, **230**, 104651, https://doi.org/10.1016/j.atmosres.2019.104651.

Morrison, H., G. Thompson, and V. Tatarskii, 2009: Impact of cloud microphysics on the development of trailing stratiform precipitation in a simulated squall line: Comparison of one- and two-moment schemes. *Mon. Wea. Rev.*, **137**, 991–1007, https://doi.org/10.1175/2008MWR2556.1.

Pan, Y., and M. Wang, 2019: Impact of the assimilation frequency of radar data with the ARPS 3DVar and cloud analysis system on forecasts of a squall line in southern China. *Adv. Atmos. Sci.*, **36**, 160–172, https://doi.org/10.1007/s00376-018-8087-5.

Parrish, D. F., and J. C. Derber, 1992: The National Meteorological Center's spectral statistical-interpolation analysis system. *Mon. Wea. Rev.*, **120**, 1747–1763, https://doi.org/10.1175/1520-0493(1992)120,1747:TNMCSS.2.0.CO;2.

Putnam, B. J., M. Xue, Y. Jung, N. A. Snook, and G. Zhang, 2017: Ensemble probabilistic prediction of a mesoscale convective system and associated polarimetric radar variables using single-moment and double-moment microphysics schemes and EnKF radar data assimilation. *Mon. Wea. Rev.*, **145**, 2257–2279, https://doi.org/10.1175/MWR-D-16-0162.1.

Roberts, N. M., and H. W. Lean, 2008: Scale-selective verification of rainfall accumulations from high-resolution forecasts of convective events. *Mon. Wea. Rev.*, **136**, 78–97, https://doi.org/10.1175/2007MWR2123.1.

Schneebeli, M., J. Sakuragi, T. Biscaro, C. F. Angelis, I. Carvalho da Costa, C. Morales, L. Baldini, and L. A. T. Machado, 2012: Polarimetric X-band weather radar measurements in the tropics: Radome and rain attenuation correction. *Atmos. Meas. Tech.*, **5**, 2183–2199, https://doi.org/10.5194/amt-5-2183-2012.

Skamarock, W. C., and Coauthors, 2008: A description of the Advanced Research WRF version 3. NCAR Tech. Note NCAR/TN-475+STR, 113 pp., https://doi.org/10.5065/D68S4MVH.

Skok, G., and N. Roberts, 2016: Analysis of Fractions Skill Score properties for random precipitation fields and ECMWF forecasts. *Quart. J. Roy. Meteor. Soc.*, **142**, 2599–2610, https://doi.org/10.1002/qj.2849.

Sokol, Z., 2011: Assimilation of extrapolated radar reflectivity into a NWP model and its impact on a precipitation forecast at high resolution. *Atmos. Res.*, **100**, 201–212, https://doi.org/10.1016/j.atmosres.2010.09.008.

Stensrud, D. J., and Coauthors, 2013: Progress and challenges with warn-on-forecast. *Atmos. Res.*, **123**, 2–16, https://doi.org/10.1016/j.atmosres.2012.04.004.

Sun, J., and Coauthors, 2014: Use of NWP for nowcasting convective precipitation: Recent progress and challenges. *Bull. Amer. Meteor. Soc.*, **95**, 409–426, https://doi.org/10.1175/BAMS-D-11-00263.1.

——, H. Wang, W. Tong, Y. Zhang, C. Lin, and D. Xu, 2016: Comparison of the impacts of momentum control variables on high-resolution variational data assimilation and precipitation forecasting. *Mon. Wea. Rev.*, **144**, 149–169, https://doi.org/10.1175/MWR-D-14-00205.1.

Testud, J., E. Le Bouar, E. Obligis, and M. Ali-Mehenni, 2000: The rain profiling algorithm applied to polarimetric weather radar. *J. Atmos. Oceanic Technol.*, **17**, 332–356, https://doi.org/10.1175/1520-0426(2000)017<0332:TRPAAT>2.0.CO;2.

Tewari, M., and Coauthors, 2004: Implementation and verification of the unified NOAH land surface model in the WRF model. *20th Conf. on Weather Analysis and Forecasting /16th Conf. on Numerical Weather Prediction*, Seattle, WA, Amer. Meteor. Soc., 14.2A, https://ams.confex.com/ams/pdfpapers/69061.pdf.

Thompson, G., P. R. Field, R. M. Rasmussen, and W. D. Hall, 2008: Explicit forecasts of winter precipitation using an improved bulk microphysics scheme. Part II: Implementation of a new snow parameterization. *Mon. Wea. Rev.*, **136**, 5095–5115, https://doi.org/10.1175/2008MWR2387.1.

Tong, W., G. Li, J. Sun, X. Tang, and Y. Zhang, 2016: Design strategies of an hourly update 3DVAR data assimilation system for improved convective forecasting. *Wea. Forecasting*, **31**, 1673–1695, https://doi.org/10.1175/WAF-D-16-0041.1.

Trémolet, Y., 2008: Computation of observation sensitivity and observation impact in incremental variational data assimilation. *Tellus*, **60A**, 964–978, https://doi.org/10.1111/j.1600-0870.2008.00349.x.

Vendrasco, E. P., J. Sun, D. L. Herdies, and C. F. de Angelis, 2016: Constraining a 3DVAR radar data assimilation system with large-scale analysis to improve short-range precipitation forecasts. *J. Appl. Meteor. Climatol.*, **55**, 673–690, https://doi.org/10.1175/JAMC-D-15-0010.1.

Wang, H., J. Sun, S. Fan, and X. Huang, 2013: Indirect assimilation of radar reflectivity with WRF 3D-Var and its impact on prediction of four summertime convective events. *J. Appl. Meteor. Climatol.*, **52**, 889–902, https://doi.org/10.1175/JAMC-D-12-0120.1.

Wolfensberger, D., and A. Berne, 2018: From model to radar variables: A new forward polarimetric radar operator for COSMO. *Atmos. Meas. Tech.*, **11**, 3883–3916, https://doi.org/10.5194/amt-11-3883-2018.

Wu, D., X. Dong, B. Xi, Z. Feng, A. Kennedy, G. Mullendore, M. Gilmore, and W. Tao, 2013: Impacts of microphysical scheme on convective and stratiform characteristics in two high precipitation squall line events. *J. Geophys. Res. Atmos.*, **118**, 11 119–11 135, https://doi.org/10.1002/jgrd.50798.

Xiao, Q., Y. Kuo, J. Sun, W. Lee, D. M. Barker, and E. Lim, 2007: An approach of radar reflectivity data assimilation and its assessment with the inland QPF of Typhoon Rusa (2002) at landfall. *J. Appl. Meteor. Climatol.*, **46**, 14–22, https://doi.org/10.1175/JAM2439.1.

Yussouf, N., E. R. Mansell, L. J. Wicker, D. M. Wheatley, and D. J. Stensrud, 2013: The ensemble Kalman filter analyses and forecasts of the 8 May 2003 Oklahoma City tornadic supercell storm using single- and double-moment microphysics schemes. *Mon. Wea. Rev.*, **141**, 3388–3412, https://doi.org/10.1175/MWR-D-12-00237.1.

Zipser, E., 1990: Rainfall predictability: When will extrapolation-based algorithms fail? *Eighth Conf. on Hydrometeorology*, Calgary, AB, Canada, Amer. Meteor. Soc., 138–142.